Electron cloud instabilities in the Proton Storage Ring and Spallation Neutron Source

M. Blaskiewicz*
Collider Accelerator Department, Brookhaven National Laboratory, 911B Upton, New York 11973-5000

M. A. Furman and M. Pivi
Center for Beam Physics, Accelerator and Fusion Research Division, Lawrence Berkeley National Laboratory, MS 71-259 Berkeley, California 94720

R. J. Macek
Los Alamos National Laboratory, P.O. Box 1663, Los Alamos, New Mexico 87545
(Received 16 October 2002; published 21 January 2003)

Electron cloud instabilities in the Los Alamos Proton Storage Ring and those foreseen for the Oak Ridge Spallation Neutron Source are examined theoretically, numerically, and experimentally.

DOI: 10.1103/PhysRevSTAB.6.014203 PACS numbers: 52.35.–g

I. INTRODUCTION

Very fast transverse instabilities have been observed in the Los Alamos Proton Storage Ring (PSR) [1–3] and, for coasting beams, in the AGS Booster [4]. Using the Booster data and the cold, coasting beam approximation for the instability growth rate, a transverse resistance of order 10 $\mathrm{M}\Omega/\mathrm{m}$ between 70 and 120 MHz is required to explain the observations. This is a large number for a ring with 200 m circumference and 6 cm pipe radius. In the PSR a broad band transverse resistance of order 1 $\mathrm{M}\Omega/\mathrm{m}$ is needed to match the observed growth rates.

A transverse, bunched beam instability has been seen in the PSR. There are several curious features, described in Sec. II, which strongly argue that the instability is due to coupled electron-proton oscillations. Electron cloud driven instabilities were observed in the ISR [5,6] and are known or suspected in several positron rings. These include the KEK photon factory [7], CESR [8], KEKB [9,10], and PEP-II [11]. For these machines the bunch length is relatively short, and much theoretical and numerical work has been done to explain the observations [7,12–16]. They have also been seen in the PS [17] and SPS [18] with proton beams. For the PSR and Oak Ridge Spallation Neutron Source (SNS) the bunches are long and a natural starting point is the application of coasting beam dispersion relations [5,6,19–21]. These dispersion relations have been applied to the PSR [1,22,23] and, recently, to the proposed J-PARC project [24]. Simulations of both coasting [25,26] and bunched beams [24,27,28] have been started. Studies based on beam breakup models [29] as well as studies of behavior well beyond threshold [30] have also been done.

This paper aims to provide an understanding of and insights into the electron cloud instability in the PSR that will be useful for a timely estimate of the impact on SNS. Parameters for the two machines are shown in Table I.

TABLE I. Machine parameters for the PSR and SNS.

Parameter	PSR	SNS
Circumference	90 m	248 m
Kinetic energy	797 MeV	1000 MeV
Nominal Q_x, Q_y	3.19, 2.12	6.3, 6.3
Beam pipe radius	5 cm	10 cm
rms emittance (x, y)	(8, 12) mm mrad	(30, 30) mm mrad
$h = 1$ rf voltage	15 kV (18 kV max)	40 kV
γ_t	3.1	5.25
High intensity	8 μC	32 μC

II. OVERVIEW OF EXPERIMENTAL DATA

The experimental characteristics of the PSR instability may be summarized as follows.

(1) The central frequency of the instability f_c increases with intensity as $f_c \propto \sqrt{I}$ [1].

(2) The PSR instability is controlled, in practice, by applying a sufficiently high rf voltage V_{rf}. For fixed bunch length τ_b the maximum number of stored protons N_b scales linearly with V_{rf} [3].

(3) The threshold value of the rf voltage for a given intensity increases when some unchopped beam is injected into the gap [3].

(4) A broad band transverse resistance of order $1\,\mathrm{M}\Omega/\mathrm{m}$ is needed to match the observed growth rates [1].

(5) For a fixed rf voltage the maximum number of stored protons depends only weakly on bunch length [1,31].

(6) Sustained, coherent oscillations are observed below the loss threshold for a well-conditioned ring.

(7) At moderate to high intensities an intense electron flux at the wall is observed as the bunch passes [32].

(8) Over accumulated operating time, for a fixed bunch intensity, the threshold rf voltage decreases [33].

 1098-4402/03/6(1)/014203(18)$20.00

(9) Increases in vacuum pressure and losses have a marginal effect on the stability threshold.

The first two items are difficult to reconcile with an impedance-driven instability since a fixed impedance should drive a given range of frequencies and given a fixed impedance the threshold intensity should scale linearly with momentum spread (or synchrotron frequency) and hence as $\sqrt{V_{\rm rf}}$.

Item (3) would be relevant to an impedance-driven instability if the beam in the gap were adequate to keep the offending resonator driven at a sufficient level. Data show that the threshold voltage doubles when ~3% of the injected turns are unchopped. In this case the ratio of the instantaneous current in the middle of the gap to the peak current is less than 2%.

Item (4) is difficult to reconcile with a machine circumference of $C = 90$ m and an average pipe radius of 5 cm.

Item (5) is at odds with both narrow and broad band impedance-driven stability models, since reducing the bunch length reduces the momentum spread in the beam.

Item (6) suggests that there is a difference between the linear threshold of the instability and the intensity required for beam loss.

Items (7) and (8) [23,32,34] are consistent with the model that has evolved to explain items (1)–(6), namely, that the instability is driven by electrons [1–4].

Figure 1 shows the threshold rf voltage as a function of beam current for different dates and a variety of injected bunch lengths. The injected bunch length is set by the width of the chopper pulse and, since the linac beam has nonzero momentum spread, is a lower limit on the bunch length in the ring. The curves are nearly straight [item (2)] and independent of bunch length [item (5)]. The historical threshold voltage lies above the curves obtained later in the run [item (8)]. The tune of the machine is quite stable, and the reduction in threshold voltage over time might be due to a reduction in secondary yield due to conditioning by electrons.

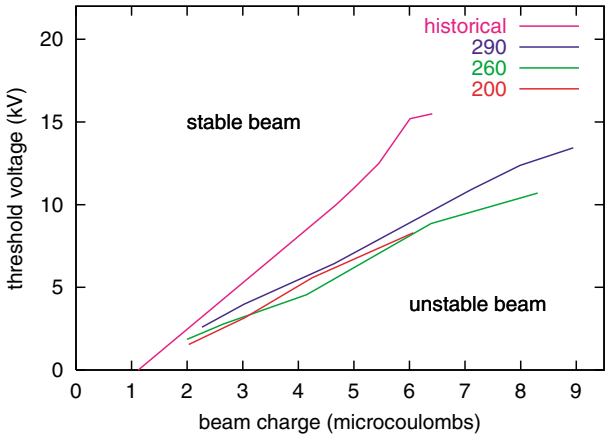

FIG. 1. (Color) Threshold rf voltage versus beam intensity. The threshold rf voltage is the smallest rf voltage for which the beam is stable. The historical curve represents the situation before the direct H^- injection upgrade and the extended run during 2001. Threshold curves near the end of the 2001 run for injected bunch lengths of 200, 260, and 290 ns are shown for comparison.

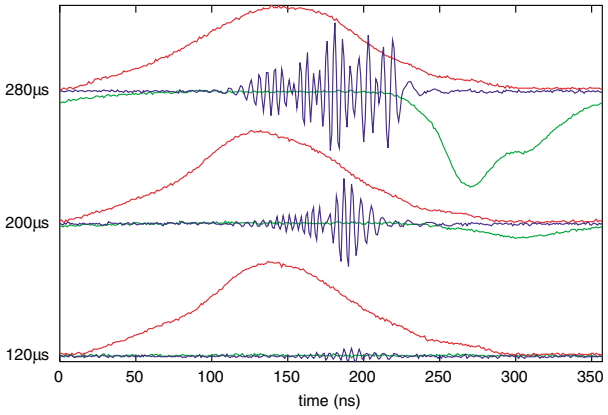

FIG. 2. (Color) Evolution of the instability for a 4.4 μC/pulse beam. The red trace is the beam current, the blue trace is a vertical beam position monitor difference signal, and the green trace is the electron current into the detector. All traces have the same time reference so one may consider all three detectors to have the same position in the ring. From bottom to top, the traces were obtained 120, 200, and 280 μs after the end of accumulation.

Evolution of the instability is shown in Fig. 2. Notice that the electron signal peaks after the instability has risen, suggesting that the electron cloud responsible for

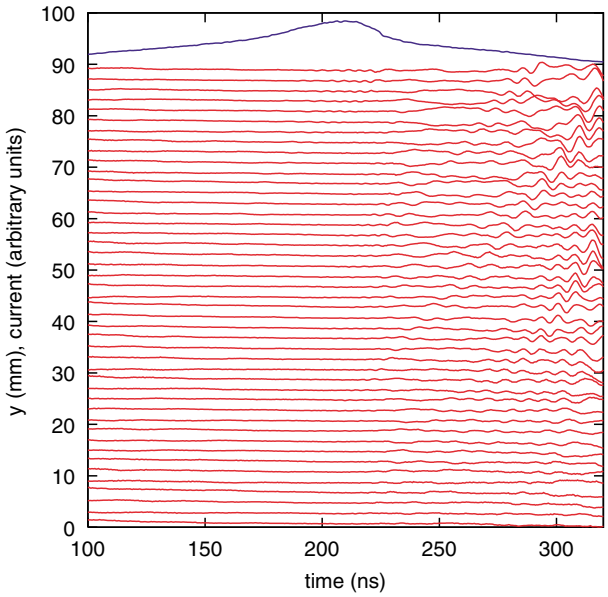

FIG. 3. (Color) Mountain range plot of transverse position along a PSR bunch (red) and the beam current (blue). The total time was 490 μs, increasing vertically, with every 30th turn plotted. The rf voltage was 10% above the threshold for fast losses.

starting the instability is not present near the detector. Other electron detectors show an observable signal before the instability begins. The electron signal represents the electron flux into the wall and gives an indication of the cloud density. This will be addressed in Sec. III.

Figure 3 shows the beam current and a mountain range plot of transverse position along the bunch. The position was obtained by integrating the sum and difference pickup signals and taking the ratio. The signal grows from noise but the amplitude saturates. These data are for a full bunch length of 275 ns and $V_{\rm rf} = 15.3$kV. Data have also been taken for shorter bunches. Persistent oscillations are present as well. The oscillations set in when $V_{\rm rf}$ is about 10% above the fast loss threshold for bunch lengths between 200 and 275 ns.

III. FORMATION OF THE ELECTRON CLOUD

The properties of the electron cloud are fundamental to the question of beam stability. An initial electron population is created by beam loss, residual gas ionization, and various processes related to the stripping foil [1,2,35]. The initial population interacts with the beam and, via secondary emission processes, is amplified. For short bunches the problem has been addressed by several authors [12,36–38]. For PSR and SNS the bunches are long and an electron trapped by the beam performs $\gtrsim 25$ transverse oscillations during a single bunch passage [39]. For electrons that exist within the beam pipe before the bunch arrives, and for those created by residual gas ionization, the electron transverse amplitude remains small during the bunch passage and multiplication via secondary emission is unlikely. On the other hand, free electrons created by losses have a transverse amplitude equal to the beam pipe radius when the instantaneous beam current is large and strike the beam pipe with appreciable energy. These processes are illustrated in Fig. 4 for typical PSR parameters.

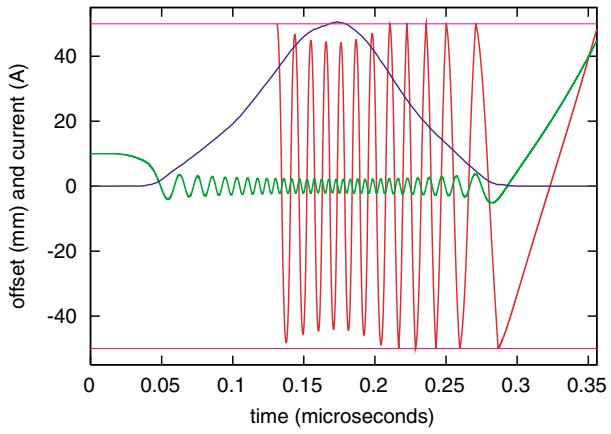

FIG. 4. (Color) Proton beam current (blue) and positions for captured (green) and loss created (red) electrons. The beam pipe radius is 50 mm (violet).

The dynamics illustrated in Fig. 4 are amenable to both analytic estimates and simulations. First we estimate the energy with which an electron can strike the wall. The electron equation of motion is approximated by

$$m_e \frac{d^2y}{dt^2} = -e\frac{Z_0 I(t)}{2\pi\beta}\frac{y}{y^2+\sigma^2}, \tag{1}$$

where y is the vertical position of the electron, $I(t)$ is the instantaneous proton beam current, $\beta = v/c$ for the protons, $Z_0 = 377\ \Omega$, and σ is the rms radius of the proton beam. Here we neglect the electric field due to the other cloud electrons. We consider motion with an amplitude comparable to the beam pipe radius b and introduce an effective frequency $\omega_e(t)$ so that the oscillator equation $\ddot{y} + \omega_e^2(t)y = 0$ has the same frequency as Eq. (1). To estimate ω_e take

$$\omega_e(t) = \sqrt{\frac{eZ_0 I(t)}{2\pi\beta m_e(\sigma^2 + 2b^2/\pi)}}, \tag{2}$$

which interpolates between small and large amplitude motion and agrees with the numerical integration of Eq. (1) to $<5\%$.

For the harmonic oscillator the adiabatically conserved action is $J = E/\omega_e(t)$ where E is the total energy. Now suppose a situation similar to the red electron line in Fig. 4. At $t \approx 0.2\ \mu$s the electron nearly hits the lower wall at $y = -b$. Half an oscillation period later the electron bounce frequency has changed by $\Delta\omega_e$ and the electron would reach an amplitude of $y = b(1 - \Delta\omega_e/2\omega_e)$ if the upper wall was absent ($\Delta\omega_e < 0$ for trailing edge electrons). The increase in amplitude yields the energy with which the electron strikes the wall. Substituting units, the electron strikes the wall with an energy

$$E_{\rm strike} = -\pi m_e c^2 \left(\frac{b}{c}\right)^2 \dot{\omega}_e/2. \tag{3}$$

The strike energy is positive on the trailing edge of the bunch ($\dot{\omega}_e < 0$) and Eq. (3) is valid only when the electron frequency does not have a large fractional change per period, $|\dot{\omega}_e| \ll \omega_e^2$. Equations (2) and (3) predict $E_{\rm strike} = 55$ eV for the strike energy. From the PSR simulation the electron has an energy of 45 eV for the first wall strike. Notice that a small error in vertical steering will cause the grazing and strike to occur on the same side of the beam pipe. For this case the strike energy is $\sim$100 eV hence amplification of the electron cloud by secondary emission is even more likely. In comparison, typical numbers for the ISIS pulsed spallation source give $E_{\rm strike} \lesssim 10$ eV for a centered beam hence no secondary amplification is expected.

Secondary emission involves the collisional liberation of electrons from within the first few tens of nanometers of the surface. Other processes such as backscatter and

rediffusion are also present. A useful experimental measure is the secondary emission yield (SEY) $\delta(E)$. For a normally incident electron with kinetic energy E, $\delta(E)$ is the average number of electrons leaving the surface due to all processes. Figure 5 shows $\delta(E)$ for titanium nitride-coated stainless steel. The samples were manufactured by the BNL vacuum group under the direction of Hseuh. The measurements were performed by Henrist of the CERN vacuum group. Notice that $\delta(0) \approx 0.8$ and is due to backscattering. The peak yield varies by $\pm 10\%$ and the peak value of $\delta(E)$ for unbaked, unconditioned, uncoated stainless steel is around 2.5.

To model the effect of a given curve the secondary yield is parametrized as

$$\delta(E) = R_0 e^{-E/E_r} + R_{\text{inf}} + \delta_{\max} \frac{s(E/E_{\max})}{s - 1 + (E/E_{\max})^s}. \quad (4)$$

The terms proportional to R_0 and R_{inf} in Eq. (4) approximate the contribution from reflected electrons while the last is due to true secondaries. For non-normal incidence the entire secondary yield is multiplied by

$$T(\theta) = e^{\alpha_\theta(1-\cos\theta)},$$

where $\cos\theta = 1$ for normal incidence and $\alpha_\theta \approx 0.5$. Electrons emitted off the surface have a range of energies and angles. For true secondaries the energy distribution is modeled by

$$P_s(E) = \frac{2E_s^2 E}{(E^2 + E_s^2)^2}.$$

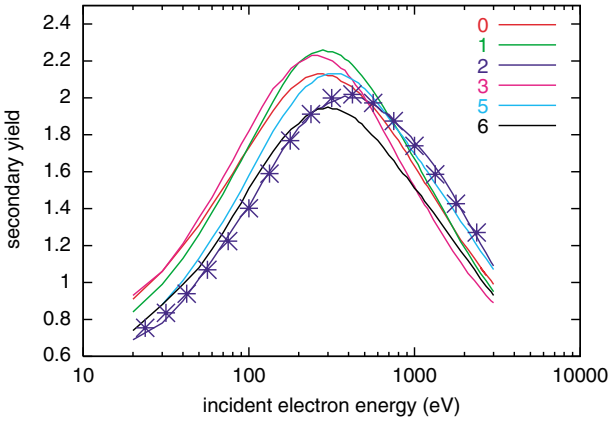

FIG. 5. (Color) Secondary emission yield for titanium nitride-coated stainless steel from identically manufactured samples. The samples were manufactured by the BNL vacuum group under the direction of Hseuh. The measurements were performed by Henrist of the CERN vacuum group. The surfaces have not been baked or conditioned in any way. The solid lines are data and the markers are a fit of Eq. (4) to the blue curve. Of all the fits, the one shown had the largest rms deviation from the data, 0.025.

Elastically reflected electrons have an energy equal to the incident energy and rediffused electrons have an energy distribution which is uniform between zero and the incident energy. The conditional probability for rediffusion $P_{r,c}$ is an input parameter.

This model has been implemented in the computer code CSEC (Cylindrically Symmetric Electron Cloud). With the wall conditions specified the simulation proceeds as follows. Initially, electron macroparticles are created at the wall. These particles are actually parallel filaments which are long compared to the pipe radius and parallel to the pipe axis. Only transverse motion is considered. At each time step the electric fields are calculated assuming constant density in the longitudinal direction. The macroparticles are produced at regular time intervals (hundreds to thousands) along the bunch and the charge on each macroparticle is proportional to the instantaneous beam intensity. The average charge liberated per meter per second is an input parameter. The beam and pipe are round and the cloud field is calculated assuming cylindrical symmetry. However, individual electron macroparticles have both radial and azimuthal velocities to include the effects of angular momentum. A drift-kick algorithm is used to update the macroparticles. When a macroparticle hits the wall the reflection probability, $P_r = [R_0 \exp(-E/E_r) + R_{\text{inf}}]\exp(\alpha_\theta[1 - \cos\theta])$, is calculated and a uniform random deviate $r1$ between 0 and 1 is chosen. If $r1 < P_r$ the macroparticle is reflected and its charge is unchanged. Another random deviate is calculated to choose between elastic and rediffused reflection and the velocity off the wall is obtained.

When $r1 > P_r$ the macroparticle charge is multiplied by

$$\frac{1}{1 - P_r} \delta_{\max} \frac{s(E/E_{\max})}{s - 1 + (E/E_{\max})^s}.$$

The macroparticle charge is compared with upper ($Q_{\max}$) and lower ($Q_{\min}$) values, which are input parameters. If the charge is less that $Q_{\min}$ the macroparticle is dropped. If the macroparticle charge is larger than $Q_{\max}$ the macroparticle is split into smaller macroparticles so that each has a charge smaller than $Q_{\max}$. For each of the macroparticles a random deviate $r2$ between 0 and 1 is chosen and the secondary energy is calculated by

$$E = E_s\left(\frac{1}{1 - r2} - 1\right)^{1/2}.$$

The velocity of the macroparticle is set to the electron velocity corresponding to E.

Given the speed of the particles off the wall, the angle between the wall normal and the velocity is chosen according to $\cos\theta = \sqrt{r3}$ where $r3$ is a uniform deviate between 0 and 1, corresponding to an angular distribution $dN/d\Omega \propto cos\theta$.

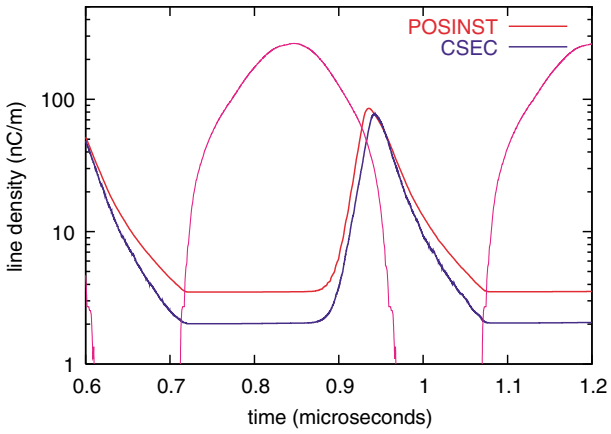

FIG. 6. (Color) Beam line density (purple) and total electron cloud line densities for the PSR obtained with CSEC (blue) and POSINST (red).

This simulation has been benchmarked against the code POSINST [40–42] for a PSR test case. Figure 6 shows the total line density for both electrons and protons. The blue line is the output of CSEC. The red line is POSINST output using the full model for the energy spectrum of the rediffused electrons. Figure 7 shows the electron current into the wall for CSEC and POSINST. For some parameters a 50% discrepancy is apparent but in the following we will show that this is small within the present context.

Table II shows the results of nonlinear least squares fitting of Eq. (4) to the curves in Fig. 5. For all but one case the best fit asymptotic reflection probability was negative, so we set $R_{\mathrm{inf}} \equiv 0$. The worst fit, with an rms error of 0.025, is shown in Fig. 5. The other SNS simulation parameters are an rms beam radius of $\sigma = 3$ cm, a primary electron production rate of 2×10^8 electrons per meter per turn, and a bunch population of 2×10^{14} protons.

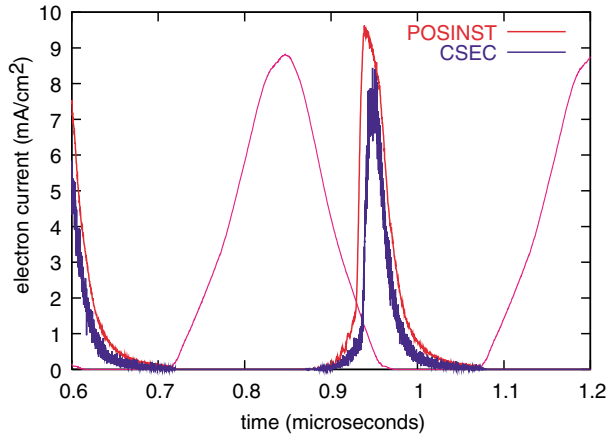

FIG. 7. (Color) Beam line density (AU) and electron current into the wall for the PSR with CSEC (blue) and POSINST (red). The beam line density, in arbitrary units, is shown to illustrate the relative timing.

TABLE II. Fitted secondary yield parameters for TiN curves in Fig. 5. The asymptotic reflection probability was set to $R_{\mathrm{inf}} \equiv 0$. The last row gives typical errors for the least squares fits.

Sample	R_0	E_r	s	$\delta_{\max}$	$E_{\max}$
0	0.66	112	1.50	2.01	317
1	0.56	129	1.56	2.20	321
2	0.50	141	1.47	1.99	433
3	0.65	60	1.56	2.22	258
5	0.50	68	1.47	2.13	331
6	0.49	157	1.50	1.88	347
Error	0.01	20	0.01	0.02	7

Simulation results for SNS are shown in Figs. 8 and 9. Figure 8 is the most relevant for stability analysis. To see this consider a round, uniform beam with line density λ_p and radius a_p, and a uniform electron cloud with line density λ_e and radius a_e. Let y be the (small) offset between the beam and cloud centroids. The force per unit length on the proton beam is

$$F_p = \frac{1}{2\pi\epsilon_0}\frac{y\lambda_p\lambda_e}{\min(a_p^2, a_e^2)} = \frac{1}{2\pi\epsilon_0}\frac{y\lambda_p}{a_p^2}\frac{\lambda_e}{\min(a_p^2/a_e^2, 1)}. \quad (5)$$

The last term on the right of (5) is the electron line density within the beam and, since a_p is nearly constant along the beam, a linear response model should use the electron line density within the beam.

Figure 9 shows the electron current into the wall. When integrated with respect to time one gets the electron dose per unit area. Table III gives the total electron dose as well as the average electron strike energy and the dose with strike energy greater than 100 eV.

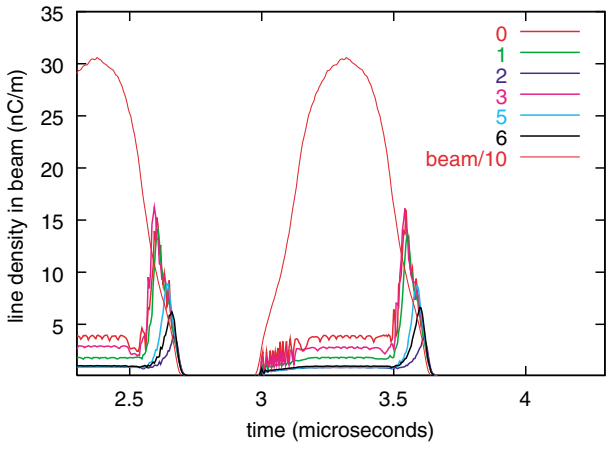

FIG. 8. (Color) SNS line charge densities for the beam and electron cloud within $r = \sigma$ for each of the six secondary yield curves in Fig. 5.

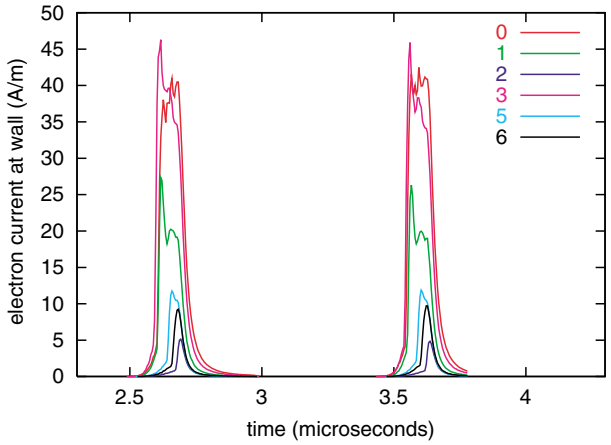

FIG. 9. (Color) SNS electron current into the wall for the simulations shown in Fig. 8. The charge deposited ranges from 40 to 700 pC/cm^2/turn.

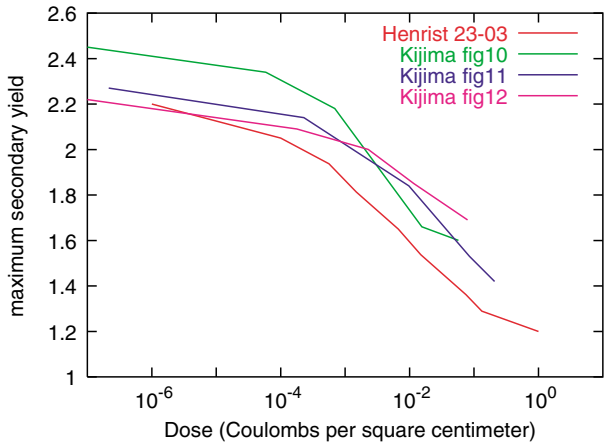

FIG. 10. (Color) Data obtained from Henrist *et al.* [43] and Kijima *et al.* [44] by using a ruler to measure the data points on the published graphs. The Henrist *et al.* data is labeled curve 23-03 in their Fig. 1. The data from Kijima *et al.* are all for $E_{\text{strike}} = 600$ eV. Kijima's Figs. 10, 11, and 12 were for OFHC, Cu-plated stainless steel, and Nb, respectively.

Over time, electrons striking the wall reduce the secondary yield. This process, known as conditioning, is a standard tool in rf and microwave engineering. Conditioning using the beam has proved beneficial in B factories, light sources, the SPS, and is important for the LHC. Figure 1 shows the benefit of conditioning for the PSR. Figure 10 shows data obtained from the articles by Henrist *et al.* [43] and Kijima *et al.* [44]. The Henrist data are for clean copper. The Kijima data are for a variety of materials. In particular, the curve for the oxygen free high conductivity copper (OFHC) surface was rinsed with water and then electron conditioned with no bake in between.

For all curves in Fig. 10 an electron dose of 0.1 C/cm^2 reduces the peak secondary yield below 1.8. For all the SEY curves in Fig. 5 the peak secondary yield is greater than 1.8 and one can reasonably expect that reducing the peak SEY to 1.8 would yield smaller densities than any shown in Fig. 8. To estimate the time required for such conditioning consider the dose with $E_{\text{strike}} > 100$ eV in Table III. Typical values are $\gtrsim 15$ pC/cm^2/turn. Simulations show that this value varies by about 50% over the last 400 turns of the 1200 turn SNS cycle, so the average dose per SNS cycle is 4.5 nC/cm^2/cycle.

TABLE III. Parameters relevant to conditioning for TiN curves in Fig. 5.

Sample	E_{strike} (eV)	Dose (pC/cm^2/turn)	Dose > 100 eV (pC/cm^2/turn)
0	24	700	43
1	36	350	39
2	61	41	10
3	24	700	45
5	49	110	22
6	56	78	17

Dividing this into 0.1 C/cm^2 and taking a 60-Hz rep rate gives a conditioning time of 106 h.

The SNS beam must be stable at reasonably high intensity for such conditioning to take place. In the following sections we consider what is known about the PSR and use various theoretical tools to extrapolate to the SNS parameter regime.

IV. LINEAR STABILITY THEORY

The stability eigenvalue problem for positron bunches in the KEKB-LER and protons in the CERN-SPS has been considered in [15,16]. A key parameter is the number of electron oscillations during the bunch passage, which is fairly small for both machines. In this case one can get good results using traditional basis expansion techniques [45] while maintaining a manageable matrix size.

For the PSR and SNS consider the beam position monitor traces in Fig. 2. The peak oscillation frequency is about $f_{\text{max}} = 200$ MHz and the bunch length is about $\tau_b = 200$ ns. Using Perevedentsev's notation [16], the smallest matrix which would allow for this fidelity involves a sum over all ℓ and $k \geq 0$ with $|\ell| + 2k \leq 2f_{\text{max}}\tau_b = 80$. This yields a 3321×3321 matrix. The eigenvalues would need to be calculated and the matrix size increased until convergence was found. Note that these matrices are dense with no special symmetry properties and a generic routine is needed [46].

An alternate technique is to model the longitudinal dynamics using a square well potential [47–49]. Particles coast longitudinally within the bunch and are reflected at both the head and the tail. The accompanying line density is a boxcar distribution and the longitudinal velocity distribution is independent of position within the

bunch. With this special distribution we will find that the dimension of the eigenvalue problem scales linearly with the number of electron oscillations within the bunch, which keeps the matrices manageable.

For zero chromaticity, the vertical equation of motion for a single proton is

$$\frac{d^2y_p}{d\theta^2} = -(Q_0^2 + Q_p^2)y_p + 2Q_0\Delta Q_{\rm sc}(y_p - \bar{y}_p) + Q_p^2\bar{y}_e. \tag{6}$$

In Eq. (6) y_p is the proton coordinate, θ is the machine azimuth which will be used as the timelike variable, Q_0 is the bare betatron tune, $\Delta Q_{\rm sc}$ is the incoherent space-charge tune shift, and $\bar{y}_e$ is the centroid position of the electron cloud which depends on both θ and longitudinal position within the bunch. The linear approximation for the space-charge force is equivalent to taking the Kapchinskij-Vladimirskij distribution for the transverse phase space density and is discussed in the Appendix.

The strength of the electron cloud interaction is determined by the parameter

$$Q_p^2 = \frac{e\lambda_e}{2\pi\epsilon_0\omega_0^2\gamma m_p \max(a_e^2, a_p^2)}, \tag{7}$$

where λ_e is the magnitude of the electron line density, ω_0 is the angular revolution frequency, a_e is the radius of the electron cloud, a_p is the radius of the proton beam, γ is the relativistic factor of the beam, and m_p is the proton mass. Notice that Q_p is the betatron tune the protons would have in the absence of other focusing forces. Let the longitudinal coordinate within the bunch be $\phi = \omega_0\tau$ with $0 < \tau < \tau_b$. As the bunch passes the electrons remain at a fixed value of θ and the electron centroid obeys

$$\frac{\partial^2\bar{y}_e(\phi,\theta)}{\partial\phi^2} + Q_e^2\bar{y}_e + 2\alpha\frac{\partial\bar{y}_e(\phi,\theta)}{\partial\phi} = Q_e^2\bar{y}_p(\phi,\theta), \tag{8}$$

where the boundary conditions are $\bar{y}_e(0,\theta) = 0$, and $\partial_\phi\bar{y}_e(0,\theta) = 0$. In Eq. (8) the transverse electron oscillation frequency is given by

$$Q_e^2 = \frac{e\lambda_p}{2\pi\epsilon_0\omega_0^2 m_e \max(a_e^2, a_p^2)}, \tag{9}$$

in analogy to (7), and the spread in electron oscillation frequency is parametrized by $\alpha \equiv Q_e/2Q_r$ with Q_r being the effective quality factor of the electron cloud. Factors contributing to this spread include variations in a_p, via variations in the lattice functions, and the dependence of the electron frequency on the electron's amplitude. Taking only lattice variations we estimate $Q_r \approx 2$ for both PSR and SNS. Integrating Eq. (8) one obtains the electron centroid,

$$\bar{y}_e(\phi,\theta) = \frac{Q_e^2}{\tilde{Q}}\int_0^\phi \bar{y}_p(\phi',\theta)\sin(\tilde{Q}[\phi-\phi'])e^{-\alpha[\phi-\phi']}d\phi', \tag{10}$$

where $\tilde{Q}^2 = Q_e^2 - \alpha^2$. Given Eqs. (6) and (10) one requires the equation for the centroid of the transverse proton position as a function of θ, ϕ, and the longitudinal momentum coordinate $v \equiv d\phi/d\theta$. Call this function $y_p(\theta,\phi,v)$.

The equation for y_p is found by making the substitution

$$\frac{d}{d\theta} \to \frac{\partial}{\partial\theta} + v\frac{\partial}{\partial\phi} - \frac{dU(\phi)}{d\phi}\frac{\partial}{\partial v}$$

in Eq. (6), where $U(\phi)$ is the longitudinal potential associated with the square well. For parameters relevant to a synchrotron, the betatron tune shifts will be small compared to the betatron tune hence we can define $y_p(\phi,v,\theta) = Y(\phi,v,\theta)\exp(-iQ_0\theta)$ and neglect second derivatives of Y. One obtains

$$\frac{\partial Y(\phi,v,\theta)}{\partial\theta} + v\frac{\partial Y}{\partial\phi} - \frac{dU(\phi)}{d\phi}\frac{\partial Y}{\partial v} = i\Delta Q_{\rm sc}[Y(\phi,v,\theta) - \bar{Y}(\phi,\theta)] + i\frac{Q_p^2Q_e^2}{2Q_0\tilde{Q}}\int_0^\phi \bar{Y}(\phi',\theta)\sin(\tilde{Q}[\phi-\phi'])e^{-\alpha[\phi-\phi']}d\phi', \tag{11}$$

where

$$\bar{Y}(\phi,\theta) = \int_{-\infty}^{\infty} dv\rho(v)Y(\phi,v,\theta),$$

with $\rho(v)$ the normalized velocity density,

$$\int_{-\infty}^{\infty} dv\rho(v) = 1.$$

Also, the approximation $Q_0^2 \approx Q_0^2 + Q_p^2$ has been used in calculating the coefficients on the right-hand side of (11).

A. Action-angle approach

The Hamiltonian for longitudinal motion is $H = v^2/2 + U(\phi)$ where $U(\phi)$ is a square well with walls at $\phi = 0$ and $\phi = \hat{\phi}$ [50]. As a proton executes a single longitudinal oscillation it encloses a phase space area of $A = 2|v|\hat{\phi}$. Define the action-angle variables I and ψ. Since I is constant and ψ increases by 2π during each oscillation, $A = 2\pi I$. In the action-angle variables the longitudinal Hamiltonian is $H = (\pi I/\hat{\phi})^2/2$. With this Hamiltonian $d\psi/d\theta \propto |v|$ so we expect $\phi = \hat{\phi}\hat{s}(\psi)/\pi$ where the sawtooth function is given by $\hat{s}(\psi) = |\psi|$ for $|\psi| < \pi$ and for other values $\hat{s}(\psi) = \hat{s}(\psi + 2\pi)$. A canonical transformation of Goldstein's third type may be

used to verify the coordinate change [51]. $F_3(\psi, v) = -v\hat{\phi}\hat{s}(\psi)/\pi$ where $\hat{\phi} = \omega_0\tau_b$. The old and new coordinates are related via

$$\phi = -\frac{\partial F_3}{\partial v} = \hat{\phi}\hat{s}(\psi)/\pi$$

and

$$I = -\frac{\partial F_3}{\partial \psi} = \hat{\phi}|v|/\pi.$$

Assume a time evolution $x = x(J, \psi)\exp(-i\Delta Q\theta)$ and consider the eigenvalue problem,

$$(\Delta Q + \Delta Q_{\rm sc})Y(\psi, I) + \frac{i\pi^2 I}{\hat{\phi}^2}\frac{\partial Y(\psi, I)}{\partial \psi} = -\int \frac{dI'd\psi'}{2Q_0} W_\perp[\phi(\psi) - \phi(\psi')]Y(\psi', I')\rho[v(I')]. \tag{12}$$

The total wake potential is given by

$$W_\perp(\phi) = -2Q_0\Delta Q_{\rm sc}\delta(\phi) + Q_p^2\frac{Q_e^2}{\tilde{Q}}\Theta(\phi)\sin(\tilde{Q}\phi)e^{-\alpha\phi}. \tag{13}$$

Next expand $Y(\psi, I)$ as

$$Y(\psi, I) = \sum_{n=-\infty}^{\infty} Y_n(I)e^{in\psi}.$$

Use Fourier orthogonality to isolate $Y_n(I)$ and define

$$\hat{Y}_n = \int_0^\infty dI' Y_n(I')\rho[v(I')].$$

Since ϕ depends only on ψ and not on I, the second line of (12) depends only on the values of $\hat{Y}_n$. Isolate the values of $\hat{Y}_n$ on the first line of (12) and define

$$A_k = \frac{\hat{Y}_k + \hat{Y}_{-k}}{1 + \delta_{k,0}},$$

where $\delta_{k,0}$ is the Kronecker delta. This yields the final dispersion relation,

$$A_k(1 + \delta_{k,0}) = \frac{-\hat{\phi}}{2\pi Q_0} D(\Delta Q + \Delta Q_{\rm sc}, k)\sum_{m=0}^{\infty} R_{k,m}A_m. \tag{14}$$

The dispersion integral is given by

$$D(\nu, k) = \int_{-\infty}^{\infty} \frac{dv\rho(v)}{\nu - k\pi v/\hat{\phi}}, \tag{15}$$

with $\nu = \Delta Q + \Delta Q_{\rm sc}$ and the impedance matrix is

$$R_{k,m} = \frac{2}{\pi}\int_0^\pi d\psi\cos(k\psi)\int_0^\pi d\psi'\cos(m\psi')W_\perp(\hat{\phi}[\psi - \psi']/\pi) = -2\pi Q_0\Delta Q_{\rm sc}\delta_{k,m}(1 + \delta_{k,0})/\hat{\phi} + \frac{Q_p^2Q_e^2}{2\hat{\phi}\tilde{Q}}{\rm Im}[G(k, m) + G(-k, m) + G(k, -m) + G(-k, -m)], \tag{16}$$

where

$$G(k, m) = \int_0^\pi d\psi\int_0^\psi d\chi e^{ik\psi + im\chi + (\psi - \chi)(i\tilde{Q} - \alpha)\hat{\phi}/\pi}.$$

For space charge $R_{k,m}$ is diagonal

$$1 = \Delta Q_{\rm sc}\int \frac{dv\rho(v)}{\Delta Q + \Delta Q_{\rm sc} - kv\pi/\hat{\phi}}. \tag{17}$$

This has the form of a coasting beam dispersion relation. Consider a wave with frequency ω_e. The value of k which creates modulations at this frequency is $k = \omega_e\tau_b/\pi$. Substituting this value and generalizing to an arbitrary coherent tune shift ΔQ_0 yields

$$1 = \Delta Q_0\int \frac{dv\rho(v)}{\Delta Q + \Delta Q_{\rm sc} - vQ_e}. \tag{18}$$

With $\Delta Q_0 = \Delta Q_{\rm sc}$ this is the dispersion relation for space-charge waves of frequency Q_e on a coasting beam with current equal to the peak current in the bunched beam.

For definiteness take $\Delta Q_0 = \Delta Q_{\rm sc}$ and a parabolic momentum distribution with $\rho(v) = (3/4\hat{v})(1 - v^2/\hat{v}^2)$ for $|v| < \hat{v}$. Equation (18) predicts a threshold for coherent oscillations which is given by

$$\frac{\Delta Q_{\rm sc}}{Q_e\hat{v}} \equiv F \geq 2/3.$$

Consider the PSR threshold for $N_p = 4 \times 10^{13}$ with $V_{\rm rf} = 15$ kV and $\tau_b = 220$ ns. Substituting these values in the last equation one obtains $F = 1.52$. Using design parameters for the SNS at 2 MW one obtains $F = 0.42$.

The space-charge threshold also scales differently from the observed behavior in PSR. Assuming that the bunch shape remains constant (i.e., parabolic) as the rf voltage and bunch length are changed, the space-charge threshold is given by

$$N_p = KV_{\rm rf}a^2\tau_b^3, \tag{19}$$

where K depends on beam energy, betatron tune, and

other machine constants. The maximum number of stored protons scales linearly with rf voltage but the scaling with bunch length does not agree with the observations.

Up to this point the calculation is equivalent to that presented in [49]. We go on to include the effects of the electron forces. Toward this end consider velocity distributions of the form [52]

$$\rho(v) = \rho_0 \prod_{j=1}^{M} \frac{1}{v^2 + \alpha_j^2} = \sum_{j=1}^{M} \frac{C_j \alpha_j}{\pi(v^2 + \alpha_j^2)}, \tag{20}$$

where $\alpha_{j+1} > \alpha_j > 0$, and the C_j's are obtained using simple matrix techniques. The shape of the distribution depends on the values of α_j chosen, with distributions approaching Gaussians being easy to construct. One such formula is

$$\alpha_j^2 = 2\sigma_G^2[M + \sqrt{M}(j-1)]\ln(1+\sqrt{M})/\sqrt{M}$$

for $j = 1, 2, \ldots, M$. For $M > 10$ the fine cancellation implied by Eq. (20) appears to require more than 16 bytes of numerical precision and we will generally use $M = 5$. The dispersion integrals (15) are given by

$$\int_{-\infty}^{\infty} \frac{\rho(v)dv}{\nu - k\pi v/\hat{\phi}} = \sum_{j=1}^{M} \frac{C_j}{\nu + i|k\pi/\hat{\phi}|\alpha_j}. \tag{21}$$

To compare these results to those of the Gaussian distribution consider the coasting beam dispersion relations $\Delta Q_0 = 1/D(\nu, 1)$ where $\hat{\phi} = \pi$ and ν varies over the real numbers. Figure 11 shows threshold curves for $M = 5$, parabolic, and Gaussian distributions with $\sigma(v) = 1$.

Substituting expression (21) for the dispersion integrals into the eigenvalue problem (14) yields

$$A_m = \sum_{j=1}^{M} \frac{C_j}{\nu + im\pi\alpha_j/\hat{\phi}} \sum_p Z_{m,p} A_p,$$

where

$$Z_{m,p} = \frac{-\hat{\phi}}{2\pi Q_0(1+\delta_{m,0})} R_{m,p}.$$

To proceed set

$$A_m = \sum_{j=1}^{M} A_{m,j}.$$

Insert this expression into the previous matrix and demand equality for each value of j, without the sum. This results in

$$\nu A_{m,j} = -i\frac{m\pi}{\hat{\phi}} \alpha_j A_{m,j} + C_j \sum_{k=1}^{M} \sum_{p=0}^{\infty} A_{p,k} Z_{m,p}. \tag{22}$$

For practical applications the infinite sum over p needs to be truncated and a value of M chosen. We will take $M = 5$ and test convergence with a simple model. Set $\omega_0 \tau_b = 2\pi/35$ and $\omega_e \tau_b = 5\pi$. The beam current and electron line density are chosen to give a cold, coasting beam tune shift of

$$\Delta Q_0 = \Delta Q_{\rm sc} + i\frac{Q_r Q_p^2}{2Q_0} = 0.10 + i00.05.$$

Plots of $\mathrm{Im}(\Delta Q)$ for the most unstable mode versus the rms tune spread in the central line $[Q_e\sigma(v)]$ for various truncation values as well as those obtained from Eq. (18) are shown in Fig. 12. Notice that the coasting beam dispersion relation gives a reasonable threshold estimate for the eigenvalue problem using the larger number of modes, $0 \le p \le 105$. Also notice that the red line takes a dip in the vicinity of $Q_e\sigma(v) = 0.015$. This dip is quite important since an accurate solution of Eq. (11) must approach the beam breakup limit as $\sigma(v) \to 0$. For the

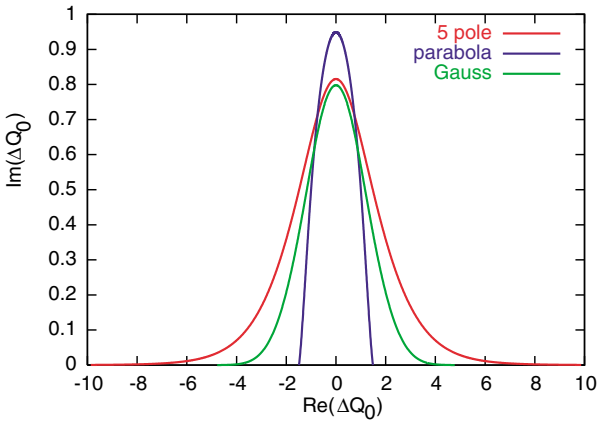

FIG. 11. (Color) Coasting beam thresholds for an $M = 5$ distribution, a Gaussian distribution, and a parabolic distribution all with $\sigma(v) = 1$.

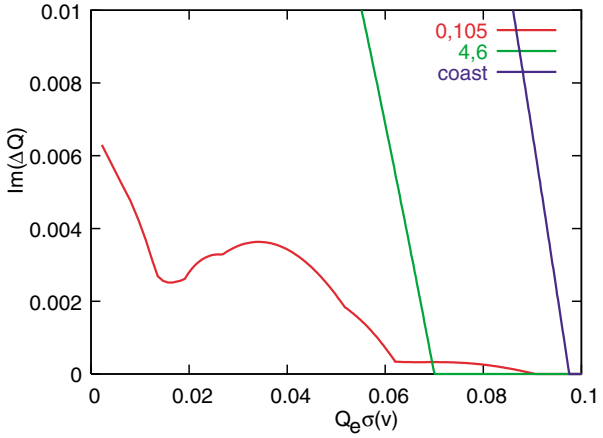

FIG. 12. (Color) Growth rate versus frequency spread for a simple model. The red and green traces are solutions to Eq. (22) with the $(0, \infty)$ summation limits on p replaced by (0105) and (4,6), respectively. The blue trace is the coasting beam threshold from Eq. (18).

beam breakup limit the amplitude of the oscillation grows as $\ln|y| \propto \sqrt{\theta}$ and as the beam breakup limit is approached the growth rates of all modes go to zero ([47], Fig. 12).

For parameter regimes appropriate to the PSR and SNS, $\omega_e \tau_b/\pi \gg 1$ and we will sum for $|p - \omega_e \tau_b/\pi| < N$. Also, for comparison to a real beam, appropriate bunch lengths and momentum spreads need to be obtained. For this we equate rms bunch length the rms momentum spread in the real and modeled beams. For the PSR a typical, real bunch length is 250 ns. When modeled by a square bunch we set $\tau_b = 177$ ns. To avoid confusion we will refer to the bunch length of the square-modeled bunch as the bunch length. Figure 13 shows results for a bunch charge of 6.4 μC and a range of PSR parameters.

The threshold voltage increases with increasing electron density, and also increases as the bunch gets shorter. The latter observation is consistent with Eq. (19). We note that $\mathrm{Im}(\Delta Q) = 0.015$ gives an equivalent transverse resistance of about 1 MΩ/m.

Figure 14 shows the threshold rf voltage versus space-charge tune shift for a bunch length of 177 ns and a bunch charge of 7 μC. The plot was made by varying ΔQ_{sc} in Eq. (13) while leaving the second term in the wakefield fixed. Space charge clearly increases the threshold voltage which also is consistent with (19). This result is different from the increase in threshold current with space-charge tune shift reported in [47]. The set of wake potentials used in [47] led to coupling between low lying modes, even with large space-charge tune shift. The wake potentials used here change sign several times allowing for coupling between high order modes. Since space charge reduces the distance between high order modes, space charge reduces the wake induced tune shift needed for coupling.

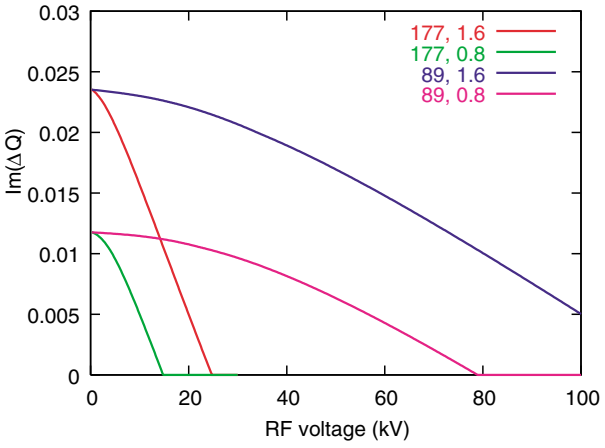

FIG. 13. (Color) Maximum growth rate versus rf voltage for PSR with 6.4 μC and various values of bunch length and electron line density.

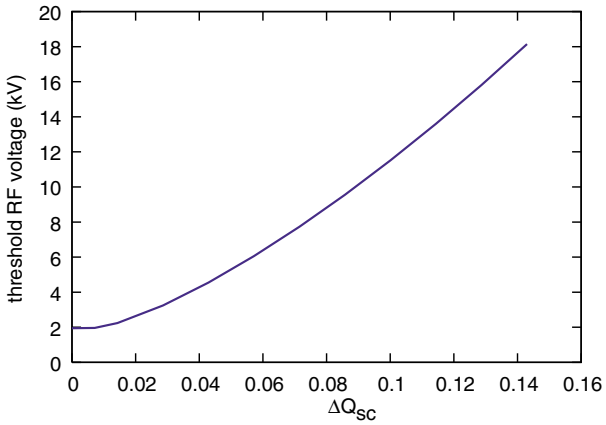

FIG. 14. (Color) Threshold rf voltage for PSR as a function of space-charge tune shift with $\tau_b = 177$ ns. The nominal value is $\Delta Q_{\mathrm{sc}} = 0.143$.

Figure 15 shows thresholds for various electron line densities and compares the matrix analysis with the coasting beam estimate. The good agreement between the two techniques suggests that a coasting beam estimate based on a more accurate momentum distribution $[\rho(v)]$ would yield a better estimate of behavior in the PSR. Figure 16 shows threshold estimates for a parabolic distribution. While the threshold estimates for small beam current are comparable in Figs. 15 and 16, the threshold voltage increases more rapidly with beam current in Fig. 16. This is a consequence of the dispersion diagrams shown in Fig. 11. The $M = 5$ dispersion curve has extended "wings" while the dispersion curve for the parabolic distribution goes to zero before a real tune shift of 2σ. This implies that the parabolic threshold is more sensitive to the space-charge tune shift, so a fair approximation to the threshold voltage can be obtained from

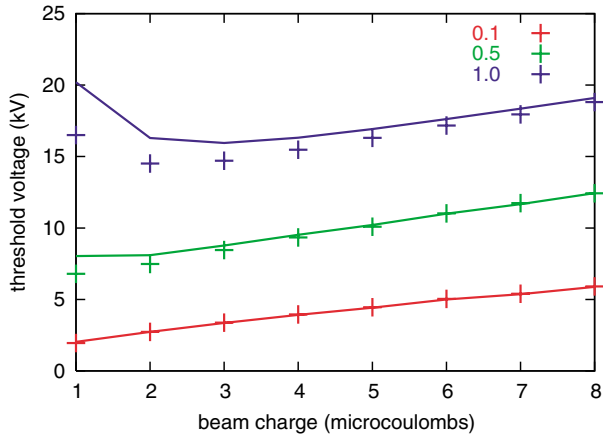

FIG. 15. (Color) Threshold voltage versus bunch charge for PSR with $\tau_b = 177$ ns, $Q_r = 2.5$, and electron line densities of 0.1 , 0.5, and 1.0 nC/m. The symbols are the thresholds for $M = 5$ and $N = 5$. The solid line is the estimate using the coasting beam dispersion relation, Eq. (18), and the $M = 5$ tune distribution.

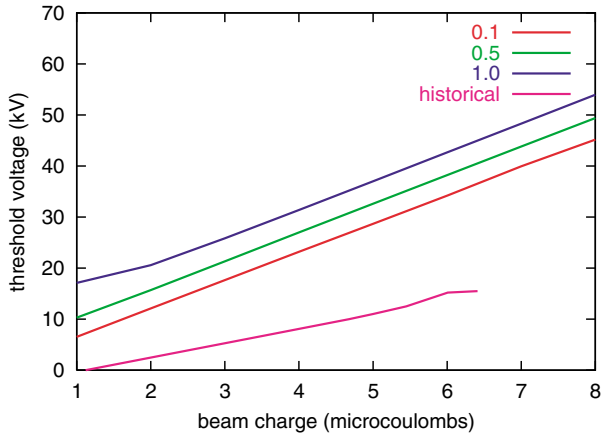

FIG. 16. (Color) Threshold voltage versus bunch charge for PSR with $\tau_b = 177$ ns, $Q_r = 2.5$, and electron line densities of 0.1 , 0.5, and 1.0 nC/m. This estimate used the coasting beam dispersion relation, Eq. (18), and a parabolic momentum distribution with the same rms width as for Fig. 15. The threshold curve for historical PSR data is shown for comparison. For the data, the momentum spread from the LINAC is present even with zero rf voltage.

Eq. (19). Also notice that Eq. (19) implies that threshold voltage increases as bunch length decreases. The factor of 3 discrepancy between theory and experiment shown in Fig. 16 becomes worse as the bunch length is reduced. Also notice that the calculated threshold voltage is a weak function of the average electron line density, which is at odds with the conditioning effects implied by Figs. 1 and 10.

Figure 17 shows results for the 2 MW SNS with the nominal space-charge tune shift $\Delta Q_{\rm sc} = 0.11$ and all

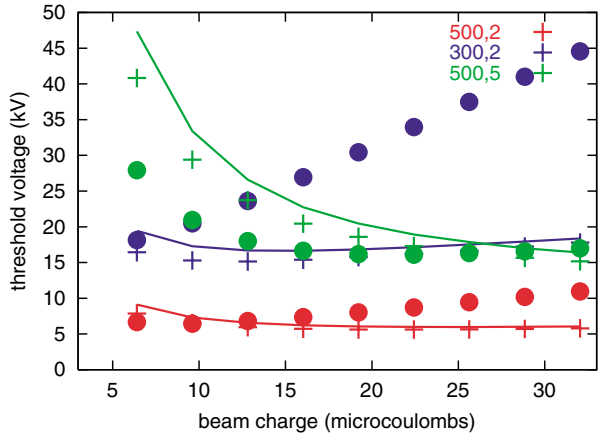

FIG. 17. (Color) Threshold voltage versus bunch charge for SNS with various values of equivalent bunch length (ns) and electron line density (nC/m), with $Q_r = 3$. The crosses are the output of the eigenvalue code with $M = 5$ and $N = 10$. The solid line is the coasting beam estimate using the $M = 5$ tune distribution. The circles are the coasting beam estimate using a parabolic momentum distribution with the same rms width.

three estimate techniques. For nominal parameters the equivalent rectangular bunch length is 500 ns and, with $\lambda_e = 2$ nC/m, the beam is stable with a harmonic 1 voltage of 10 kV. The design voltage is 40 kV.

B. Nonlinear space-charge forces

For the PSR the transverse beam profile is roughly Gaussian. SNS target requirements dictate a transverse density that is nearly constant within the beam and a sharp beam edge. This implies that the transverse amplitude dependence of the space-charge tune shift in the PSR is significantly larger than in the SNS. The impact of this difference on instability threshold estimates for the PSR is the subject of the present section.

Consider a coasting beam instability and take the evolution variable to be time (t). Consider only one transverse dimension ($y, v = \dot{y}$). Take the fractional momentum deviation, $\delta = (p - p_0)/p_0$, to be the longitudinal momentumlike coordinate and θ to be the longitudinal position coordinate. The equation for the electron centroid is approximated as

$$\frac{\partial^2 \bar{y}_e(\theta, t)}{\partial t^2} + \frac{\omega_e}{Q_r}\frac{\partial \bar{y}_e}{\partial t} = \omega_e^2(\bar{y}_p - \bar{y}_e). \tag{23}$$

For no momentum spread the proton centroid obeys

$$\left[\frac{\partial}{\partial t} + \omega_0 \frac{\partial}{\partial \theta}\right]^2 \bar{y}_p(\theta, t) + \omega_\beta^2 \bar{y}_p = \omega_p^2(\bar{y}_e - \bar{y}_p). \tag{24}$$

Set $\bar{y}_p = \hat{y}_p \exp[ik(\omega_0 t - \theta) + i\omega_c t]$ and $\bar{y}_e = \hat{y}_e \exp[ik(\omega_0 t - \theta) + i\omega_c t]$. Assume that $|k\omega_0 - \omega_c - \omega_e| \ll \omega_e/Q_r$ so that $\hat{y}_e = -iQ_r\hat{y}_p$. Additionally assume that $|\omega_c - \omega_\beta| \ll \omega_\beta$ so that coupling to the other betatron sideband can be ignored. Then $\omega_c - \omega_\beta = i\omega_p^2 Q_r/2\omega_\beta$ is the coherent frequency shift of the protons. Next consider momentum spread in the absence of collective forces. For a particle with momentum offset δ its kth betatron sideband occurs at a frequency

$$\omega_k(\delta) = k\omega_0(1 - \eta\delta) - (1 - \eta\delta + \xi\delta)\omega_\beta,$$

where $\eta = 1/\gamma^2 - 1/\gamma_t^2$, ξ is the normalized chromaticity, and ω_β is the betatron frequency for an on-momentum particle in the absence of collective effects [53]. The frequency spread in the beam is given by the momentum distribution, $\rho(\delta)$, and the relation

$$\delta\omega_\beta(\delta) = \eta(k\omega_0 - \omega_\beta)\delta + \xi\omega_\beta\delta \approx -\eta\omega_e\delta.$$

We may now use the formalism in [52] to estimate the effects of nonlinear space charge on stability thresholds. Considering the results of the previous section we take a parabolic momentum distribution with half-width at base $\delta_{\rm max}$, and numerically calculate Eq. (33) in [52]. Figure 18 shows stability diagrams for a generic coherent tune shift and various amounts of space charge. The parameter $W = \delta\omega_\beta(\delta_{\rm max})/\omega_0$ is the normalized frequency spread in the

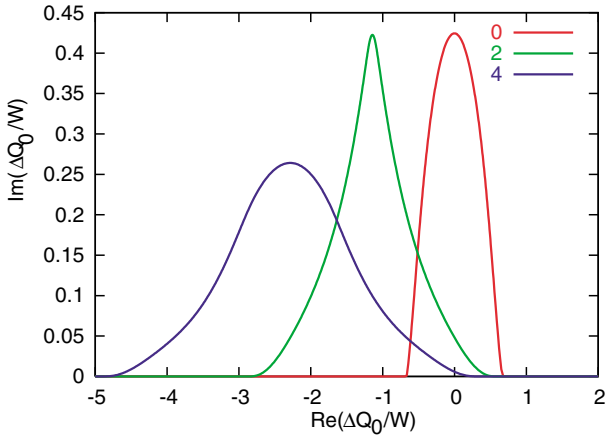

FIG. 18. (Color) Threshold diagrams for various values of $\Delta Q_{\mathrm{sc,max}}/W$ and highly nonlinear space charge with $q/\kappa = 3/5$. Tune shifts corresponding to points below a given curve are stable for that value of $\Delta Q_{\mathrm{sc,max}}/W$.

sideband due to momentum spread, and the curves are labeled according to the central space-charge tune shift via $\Delta Q_{\mathrm{sc,max}}/W$. These curves assume a round beam with transverse density proportional to $(r_{\mathrm{max}}^2 - r^2)^2$ with nonlinearity parameter $q/\kappa = 3/5$ [52]. This regime corresponds to a soft upper limit for space-charge tune spread in real beams and yields a tune shift with betatron amplitude ($\hat{y}$) that is given by

$$\Delta Q_{\mathrm{sc}}(\hat{y}) = \Delta Q_{\mathrm{sc,max}}\left[1 - \frac{6}{13}\left(\frac{\hat{y}}{\hat{y}_{\mathrm{max}}}\right)^2\right]. \qquad (25)$$

For our purposes the width of the tune distribution is $W = \delta_{\mathrm{max}}|\eta|Q_e$. By any measure, $\Delta Q_{\mathrm{sc}} \gg Q_r Q_p^2/2Q_\beta$, so the coherent tune shift is $\Delta Q_0 = iQ_r Q_p^2/2Q_\beta$. Figure 19 shows threshold voltage versus beam current

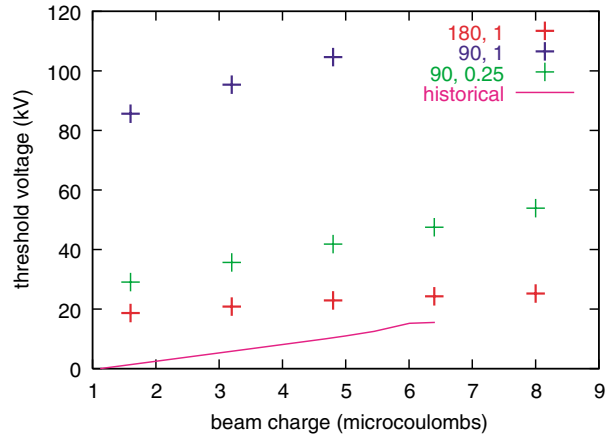

FIG. 19. (Color) PSR threshold voltage versus bunch charge for rms bunch lengths of 180 and 90 ns and electron line densities of 1 and 0.25 nC/m, with an rms emittance of 8.5 mm mrad. The symbols are for maximal space-charge tune spread with $q/\kappa = 3/5$ and the solid line is the historical PSR data.

for long and short bunches with maximal space-charge tune spread.

For both bunch lengths the threshold voltage with nonlinear space charge is no larger than the threshold assuming linear space-charge forces. Also notice that the threshold voltage for the short bunch is significantly reduced when the electron line density is reduced. The value of 0.25 nC/m was in fact calculated using CSEC with a 7 μC bunch and wall parameters consistent with partially conditioned stainless steel. The large reduction in threshold voltage due to reduced λ_e is in sharp contrast to the results in Fig. 16.

The possibility that threshold voltage is a strong function of electron survival during the gap has been suggested before, and the conjecture that it influences the dependence of threshold voltage on bunch length has been made [1,31]. There are other experimental facts that have not been included in the calculations leading to the figures. The electron line density surviving the gap is a strong function of bunch current [33]. Also, the threshold scaling like τ_b^0 in Fig. 1 is different from earlier observations, which showed something more like τ_b^{-1} [1,2]. That is to say the fact that the curves for different bunch lengths are essentially identical in Fig. 1 does not indicate a fundamental symmetry of the physics. Finally, from Fig. 2 it is clear that the electron cloud responsible for the onset of the instability does not always occupy the entire ring.

By including these sorts of effects it might be possible to fit both the intensity and bunch length scaling in PSR. Instead, we will remember that the model used here is fairly rough and attack the problem using simulations.

V. SIMULATIONS

A. Description of algorithms

The parameter regimes appropriate to the PSR and SNS make a direct particle in cell calculation of the electron cloud instability difficult. In this section we develop some phenomenological equations of motion which contain the various interactions in simplified form that allow for greater computational speed. Consider a single proton macroparticle. The continuum version of its equations of motion is taken to be

$$\frac{d^2\tau_p}{d\theta^2} = -Q_s^2\tau_p, \qquad (26)$$

$$\frac{d^2y_p}{d\theta^2} = -Q_y^2 y_p + C_{\mathrm{sc}}(\theta,\tau)[y_p - \bar{y}_p(\theta,\tau)] + F_{y,e}(y_p,\theta,\tau), \qquad (27)$$

$$\frac{d^2x_p}{d\theta^2} = -Q_x^2 x_p. \qquad (28)$$

The longitudinal coordinate is arrival time, τ_b, and the

motion is simple harmonic with synchrotron tune Q_s. The vertical motion has bare tune Q_y, with transverse, linear space-charge forces and a vertical force on the proton due to the electron cloud $F_{y,e}$. The assumption of linear transverse space charge increases computational speed. From Figs. 18 and 19 this approximation could significantly underestimate threshold current for PSR. The horizontal motion is unperturbed with betatron tune Q_x. Neglecting the horizontal collective forces roughly halves the simulation time though they could easily be included. The code actually allows for nonzero chromaticity, but its effect is negligible for PSR and SNS parameter regimes.

Electron macroparticles are assumed to have transverse motion only. When the macroparticle is inside the pipe

$$\frac{d^2 y_e}{d\tau^2} = F_{y,p}(y_e, \theta, \tau) + \kappa F_{y,e}(y_e, \theta, \tau), \tag{29}$$

$$\frac{d^2 x_e}{d\tau^2} = I_d[F_{x,p}(y_e, \theta, \tau) + \kappa F_{x,e}(y_e, \theta, \tau)]. \tag{30}$$

The vertical force on an electron macroparticle is due to both the protons $F_{y,p}$ and the electron cloud $\kappa F_{y,e}$. When nonzero, the parameter κ accounts for the mass ratios as well as the fact that the proton timelike variable is taken to be azimuth (θ), while the electrons evolve in real time during the passage of the proton bunch. Horizontal electron motion is analogous to the vertical for motion in a drift ($I_d = 1$). For motion in a dipole magnet the horizontal/longitudinal Larmor motion is neglected and $I_d = 0$. Wall interactions will be discussed later.

The continuum version of the collective force on the electrons due to the protons is taken to be

$$\mathbf{F}_p = \frac{e\lambda_p(\theta, \tau)}{2\pi\epsilon_0 m_e} \frac{[a(\theta)/a_0]\bar{\mathbf{x}}_p(\theta, \tau) - \mathbf{x}_e}{\min\{a(\theta)^2, |[a(\theta)/a_0]\bar{\mathbf{x}}_p(\theta, \tau) - \mathbf{x}_e|^2\}}. \tag{31}$$

The actual beam radius $a(\theta)$ is allowed to vary with azimuth as appropriate to a strong focusing machine. This means that $\mathbf{x}_p$ is actually the normalized position coordinate and θ is the phase advance divided by the tune. The proton beam is assumed to be round which simplifies the electron update equations. The value $a(\theta)$ is an input function, not derived from the beam characteristics, with $a(\theta) = a(\theta + 2\pi)$. The range of values of $a(\theta)$ reproduces the variation in electron bounce frequency for the actual lattice calculated using variations in both the horizontal and vertical beam dimensions.

To get the collective force on the protons due to the electrons the average and mean square positions of the cloud are obtained for each azimuth and each time step along the bunch. Let the macroparticles be denoted by index j, then

$$\bar{\mathbf{y}}_e(\theta, \tau) = \frac{\sum_j \lambda_{e,j}\mathbf{y}_{e,j}}{\sum_j \lambda_{e,j}}, \tag{32}$$

$$\sigma_e^2(\theta, \tau) = \frac{\sum_j \lambda_{e,j}[\mathbf{y}_{e,j} - \bar{\mathbf{y}}_e(\theta, \tau)]^2}{\sum_j \lambda_{e,j}}. \tag{33}$$

The average and variance are then multiplied by $a_0/a(\theta)$ and $[a_0/a(\theta)]^2$, respectively, to account for the normalized proton coordinates. The macroparticles can have different charges (actually line densities) due to interactions with the walls. The force on the protons due to the electrons is

$$F_{y,e}(y_p, \theta, \tau) = \frac{e\lambda_e(\theta, \tau)}{2\pi\epsilon_0 m_p \gamma \omega_0^2}\left[\frac{\bar{y}_e(\theta, \tau) - y_p}{\sigma_e^2(\theta, \tau) + |\bar{\mathbf{x}}_e(\theta, \tau) - \mathbf{x}_p|^2}\right]. \tag{34}$$

The initial conditions of the electron cloud and secondary emission are considered as follows. For each azimuth at which the beam is updated, usually 10 times per betatron oscillation, the electron cloud is generated by taking N_e electron macroparticles with random positions within the pipe and zero velocity. Each macroparticle has the same initial line density and their sum is an input parameter, λ_e. A given macroparticle is evolved by Eqs. (29) and (30) until it strikes the wall with energy E. Upon striking the wall Eq. (4) is evaluated and that macroparticles charge is multiplied by the secondary emission yield $\delta(E)$. After the charge is updated the macroparticle remains in the same location, but with zero velocity. This neglects the complications associated with the secondary energy distribution and should have a small effect on the proton dynamics.

To discretize the equations of motion we take $\sim 10\ Q_y$ equally spaced thin lenses in machine azimuth to implement the collective forces. Between collective kicks the transverse and longitudinal proton motions are approximated by rotation matrices. Consider the implementation of the collective forces at a given thin lens. Choose a longitudinal smoothing length τ_e and a longitudinal bin size $\delta\tau = T_{\text{rev}}/N_g$. Generally $\tau_e/\delta\tau \gtrsim 10$ and $\omega_e\tau_e < 1$, where ω_e is the maximum value of the electron bounce frequency within the bunch. Use linear interpolation to calculate estimates of $\lambda_p(\tau)$ and $\lambda_p(\tau)\bar{y}_p(\tau)$ on the N_g grid points. Smooth these arrays using $S(t) = (1 + 4|t|/\tau_e)\exp(-4|t|/\tau_e)/\tau_e$ which involves one exponentiation and $O(N_g)$ additions and multiplications when the convolution is expressed as an autoregressive filter. The smoothed values $\lambda_p(\tau)$ and $\bar{y}_p(\tau)$ (obtained by division) are used to drive the electron cloud via Eqs. (29)–(31). As the proton bunch passes, Eqs. (32) and (33) and the electron line density $\lambda_e(\tau)$ are stored in arrays. Then Eq. (34) is used to get the transverse kicks on each of the proton macroparticles.

B. Results

The simulation code has five purely numerical parameters and 14 physical parameters. Fiducial values for these

TABLE IV. Nominal simulation parameters for the PSR and SNS.

Parameter	PSR	SNS
Circumference	90 m	248 m
Revolution period	357 ns	945 ns
Beam kinetic energy	797 MeV	1000 MeV
Betatron tunes Q_x, Q_y	3.16, 2.14	6.2, 6.2
Pipe radius	5 cm	10 cm
Beam radius (a_0)	1.5 cm	2.8 cm
Maximum synchrotron tune Q_s	7.1×10^{-4}	9.4×10^{-4}
Maximum bunch charge	8 μC	32 μC
$\delta_{\max}$	2.0	2.0
$E_{\max}$	300 eV	300 eV
Full bunch length	270 ns	700 ns
$I_{\text{peak}}/I_{\text{avg}}$	2.9	2.0
$\Delta\omega_{e,\text{full}}/\omega_e$ [via $a(\theta)$]	0.5	0.5
λ_e	1 nC/m	2 nC/m
Updates/turn	20	60
Proton macroparticles, M_p	6×10^5	5×10^6
Electron macroparticles, M_e	20	20
Smoothing length, τ_e	0.25 ns	0.25 ns
Longitudinal bins, $T_{\text{rev}}/\delta t$	64 000	64 000

are given in Table IV. To characterize the evolution during the simulation consider the average value of the coherent amplitude on turn n, $Y(n)$. Define

$$\bar{p}_p(\theta, \tau) = \langle (1/Q_y)(dy_p/d\theta) \rangle,$$

in direct analogy to $\bar{y}_p(\theta, \tau)$. For turn n

$$[Y(n)]^2 \equiv \frac{\int_0^{T_{\text{rev}}} d\tau \lambda_p(2\pi n, \tau)[\bar{y}_p^2(2\pi n, \tau) + \bar{p}_p^2(2\pi n, \tau)]}{\int_0^{T_{\text{rev}}} d\tau \lambda_p(2\pi n, \tau)}. \tag{35}$$

Figure 20 shows the evolution of Y for the SNS and PSR parameters in Table II. The PSR is unstable and losses on the tail of the bunch are apparent in Fig. 21. There is no simulation flag associated with a proton hitting the pipe wall so behavior after the beam gets outside the pipe is unphysical. Figure 22 shows the PSR current pulse and the dipole density, $I(\tau)\bar{y}_p(\tau)$. The rms amplitude of 3 mm would produce an easily measurable instability signal. The same parameters for SNS are plotted in Fig. 23. The dipole density corresponds to the $Y \sim 0.5$ mm amplitude displayed by SNS throughout the simulation. There is no sign of instability in this case.

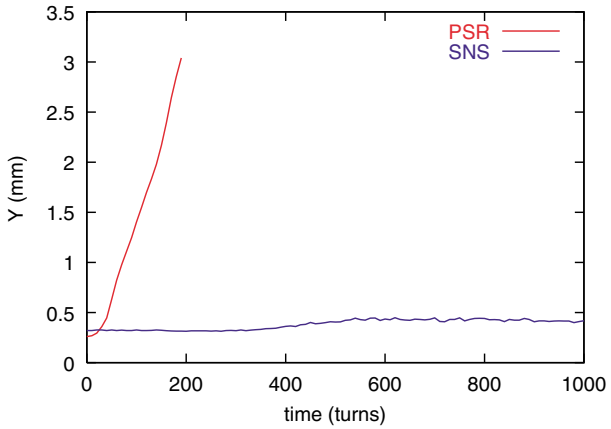

FIG. 20. (Color) Evolution of Y for PSR and SNS parameters in Table II.

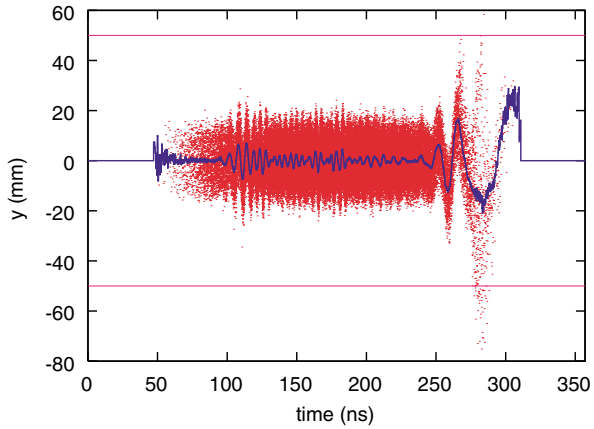

FIG. 21. (Color) Macroparticles and smoothed offset for the last turn of the PSR simulation using parameters in Table II. The vertical aperture is shown too.

The PSR parameters in Table II correspond to a marginally stable beam in the actual PSR, while the simulation predicts a strong instability. Simulations of the PSR for other intensities, bunch lengths, and rf voltages have been done. In general, the onset of the instability roughly corresponds to the coasting beam estimates for parameters in the middle of the bunch. This is not the same as equating rms quantities, since the longitudinal profile of the PSR beam is typically quite peaked. The simulations also show some evidence of nonlinear saturation, which is not surprising given Eq. (34). However, for such nonlinear saturation to play a fundamental role in the PSR

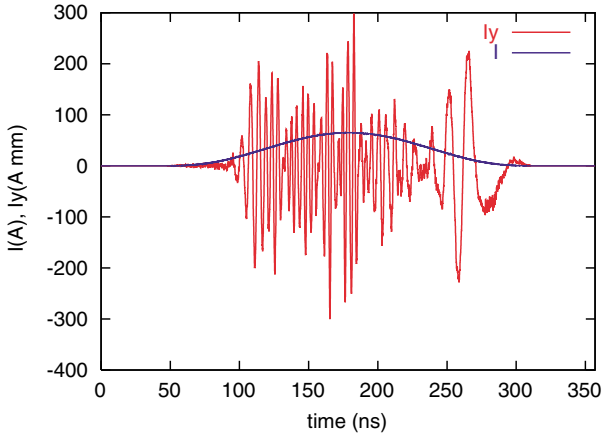

FIG. 22. (Color) Instantaneous current and dipole density for the 200th turn of PSR simulation using parameters in Table II.

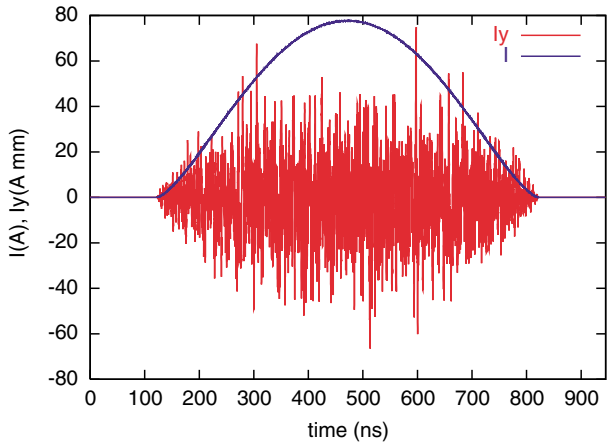

FIG. 23. (Color) Instantaneous current and dipole density for the 1000th turn of SNS simulation using parameters in Table II.

it would be necessary to observe the linear threshold of the instability at intensities well below those required for beam losses. This would be especially true for short bunches and it is not observed in the actual machine.

For SNS, the rms bunch length is a good indicator of peak current. The simulations agree fairly well with the thresholds show in Fig. 17.

VI. CONCLUSIONS

Electron cloud instabilities in the PSR and SNS have been explored. Estimates of the SNS cloud density have been made using measured secondary yield data. For 2×10^{14} protons per bunch we expect less than 5 nC/m of electrons to survive the gap. Similar simulations have been done for the PSR and agree well with experiments. Linear stability theory has been applied to the PSR and SNS. For the PSR, the linear model tends to predict instability for lower currents than are actually observed. This may in part be due to our conservative approximations. For the SNS with 2×10^{14} protons per bunch, the linear theory predicts that a harmonic-one rf voltage of 15 kV should be adequate to stabilize the beam for an electron density of 5 nC/m. The harmonic-one design voltage for SNS is 40 kV. Simulations of the electron cloud instability have been performed. For SNS, the simulations are in fair agreement with the predictions of the linear stability analysis. With 2×10^{14} protons per bunch and a 60 Hz repetition rate, conditioning rates for electrons with more than 100 eV of kinetic energy are $(0.1 \rightarrow 0.5)$ C/cm^2/week for the unconditioned surfaces considered here. A dose of 0.1 C/cm^2 should reduce the peak secondary yield to 1.8 or less.

ACKNOWLEDGMENTS

This work has benefited from conversations with P. Channell, V. A. Danilov, R. Davidson, K. Harkay, G. Lambertson, Y. Y. Lee, H. Qin, T. S. Wang, J. Wei, and S. Y. Zhang. Special thanks to the BNL vacuum group, under the direction of H. C. Hseuh, for preparing the titanium nitride-coated samples and the CERN vacuum group for measuring the secondary yield. M. B.'s work was funded by the SNS project. SNS is managed by UT-Battelle, LLC, under Contract No. DE-AC05-00OR2275 for the U.S. Department of Energy. SNS is a partnership of six national laboratories: Argonne, Brookhaven, Jefferson, Lawrence Berkeley, Los Alamos, and Oak Ridge. M. A. F. and M. P. are grateful to NERSC for supercomputer support. Their work was supported by the U.S. DOE under Contract No. DE-AC03-76SF00098 and by the SNS project. R. J. M.'s work was conducted in part by the Los Alamos National Laboratory, which is operated by the University of California for the U.S. DOE under Contract No. W-7405-ENG-36.

APPENDIX: MOTIVATION FOR THE LINEAR SPACE-CHARGE TERM

To motivate the linear space-charge term in Eq. (6) consider the coupled Vlasov-Maxwell equations for a beam in a straight channel with uniform, linear focusing. We use (x, y, z) and (p_x, p_y, p_z) as the phase space coordinates and clock time t as the evolution variable, with $F(x, y, z, p_x, p_y, p_z, t)dxdydzdp_xdp_ydp_z$ denoting the total charge in the phase space volume $dxdydzdp_xdp_ydp_z$. The particle velocity is $d\mathbf{r}/dt = \mathbf{v} = \mathbf{p}/\gamma m$ and q is the charge per particle.

The Vlasov equation is given by

$$\frac{\partial F}{\partial t} + \mathbf{v} \cdot \frac{\partial F}{\partial \mathbf{r}} + q\{\mathbf{E}(\mathbf{r}, t) + \mathbf{v} \times \mathbf{B}(\mathbf{r}, t)\} \cdot \frac{\partial F}{\partial \mathbf{p}} = 0, \quad \text{(A1)}$$

where $\mathbf{E}(\mathbf{r}, t)$ and $\mathbf{B}(\mathbf{r}, t)$ are the electric and magnetic fields as a function of position and time.

Since Maxwell's equations are linear we may split the electric and magnetic fields in the form $\mathbf{E} = \mathbf{E}_0 + \mathbf{E}_1$, where $\mathbf{E}_0$ is the electric field for a perfectly conducting pipe and $\mathbf{E}_1 = \mathbf{E} - \mathbf{E}_0$ is the field due to wall impedance, electron cloud, quadrupoles, and rf cavities. Similarly we set $\mathbf{B} = \mathbf{B}_0 + \mathbf{B}_1$. We will call $\mathbf{E}_0$ and $\mathbf{B}_0$ the space-charge fields. To proceed we work in the Lorentz gauge

$$\mathbf{E}_0 = -\nabla\Phi - \frac{\partial \mathbf{A}}{\partial t}, \quad \text{(A2)}$$

$$\mathbf{B}_0 = \nabla \times \mathbf{A}, \quad \text{(A3)}$$

$$\nabla^2\Phi = \frac{1}{c^2}\frac{\partial^2\Phi}{\partial t^2} - \frac{\rho}{\epsilon_0}, \quad \text{(A4)}$$

$$\nabla^2\mathbf{A} = \frac{1}{c^2}\frac{\partial^2\mathbf{A}}{\partial t^2} - \mu_0\mathbf{J}, \quad \text{(A5)}$$

$$\nabla \cdot \mathbf{A} = -\frac{\partial\Phi}{\partial t}. \quad \text{(A6)}$$

Let $\mathbf{v}_0 = \hat{z}v_0$ be the velocity of the synchronous particle and make the approximation

$$\mathbf{J} \approx \hat{z}v_0\rho(\mathbf{r}, t). \tag{A7}$$

This is equivalent to neglecting the transverse beam velocity and, for longitudinal wavelengths λ_z, results in a fractional error of order $(a/\gamma\lambda_z)^2$ [54]. To the same order of approximation take

$$\mathbf{E}_0 + \mathbf{v} \times \mathbf{B}_0 \approx \mathbf{E}_0 + v_0\hat{z} \times \mathbf{B}_0. \tag{A8}$$

With these approximations

$$\mathbf{E}_0(\mathbf{r}, t) + \mathbf{v} \times \mathbf{B}_0(\mathbf{r}, t) = -\frac{\nabla\Phi}{\gamma^2}. \tag{A9}$$

Note that (A9) holds for both transverse and longitudinal fields. The equation for Φ is given by

$$\nabla_\perp^2\Phi + \frac{\rho}{\epsilon_0} = \frac{1}{c^2}\frac{\partial^2\Phi}{\partial t^2} - \frac{\partial^2\Phi}{\partial z^2} \approx \frac{-1}{\gamma^2}\frac{\partial^2\Phi}{\partial z^2} \approx 0, \tag{A10}$$

where $\nabla_\perp = (\partial/\partial x, \partial/\partial y)$ is the gradient with respect to the transverse variables. Neglecting the derivatives with respect to z and t is equivalent to assuming that longitudinal variations in the rest frame of the bunch have a length scale much larger than the vacuum chamber radius. Note that Eqs. (A7)–(A10) form the basis for several space-charge simulation codes [55].

We are interested in the transverse forces so we split the space-charge terms

$$-\nabla_\perp\Phi(x, y, z, t) = \frac{1}{2\pi\epsilon_0}\int d^2x'_\perp \rho(\mathbf{x}'_\perp, z, t)\frac{\mathbf{x}_\perp - \mathbf{x}'_\perp}{|\mathbf{x}_\perp - \mathbf{x}'_\perp|^2} + \text{image terms}, \tag{A11}$$

where $\mathbf{x}_\perp = (x, y)$ is the two-dimensional transverse position vector, and we absorb the image terms into $\mathbf{E}_1$ and $\mathbf{B}_1$.

Both the lattice and image parts of $\mathbf{E}_1$ and $\mathbf{B}_1$ can have a nonlinear dependence on $\mathbf{x}_\perp$. We will neglect these nonlinearities here. Also we will make a uniform focusing approximation so that the net force in Eq. (A1) is given by

$$\{\mathbf{E}(\mathbf{r}, t) + \mathbf{v} \times \mathbf{B}(\mathbf{r}, t)\} = -\frac{\nabla\Phi}{\gamma^2} - k_x x\hat{x} - k_y y\hat{y} + \hat{z}E_z(z - v_0 t) + \hat{x}\mathcal{E}_x(z, t) + \hat{y}\mathcal{E}_y(z, t), \tag{A12}$$

where hats denote unit vectors, k_x and k_y are the quadrupole focusing terms, $E_z(z - v_0 t)$ is the longitudinal electric field in the smooth approximation, and $\mathcal{E}$ is the $\mathbf{E} + \mathbf{v} \times B$ field due to images and wall impedance.

Redefine the longitudinal variables to be $\tilde{z} = z - v_0 t$ and $\delta = (p_z - p_0)/p_0$. Define

$$\Psi_0(\delta, \tilde{z}, t) = \int d^2p_\perp d^2x_\perp F(\mathbf{x}_\perp, \mathbf{p}_\perp, \tilde{z}, \delta, t).$$

Integrating Eq. (A1) over the transverse variables yields

$$\frac{\partial\Psi_0}{\partial t} + v_0\frac{\delta}{\gamma^2}\frac{\partial\Psi_0}{\partial\tilde{z}} + \frac{qE_z(\tilde{z})}{p_0}\frac{\partial\Psi_0}{\partial\delta} \equiv \frac{d\Psi_0}{dt} = 0, \tag{A13}$$

where we define the longitudinal, convective derivative. The transverse motion is decoupled and we take the time independent solution $\Psi_0(\tilde{z}, \delta) = G[\delta^2/2 + \tilde{U}(\tilde{z})]$, where G defines the stationary longitudinal distribution and $d\tilde{U}/dz = -\gamma^2 qE_z/p_0 v_0$. Define two more moments

$$\mathbf{D}(\tilde{z}, \delta, t) = \int d^2p_\perp d^2x_\perp \mathbf{x}_\perp F(\mathbf{x}_\perp, \mathbf{p}_\perp, \tilde{z}, \delta, t), \tag{A14}$$

$$\mathbf{P}(\tilde{z}, \delta, t) = \int d^2p_\perp d^2x_\perp \mathbf{p}_\perp F(\mathbf{x}_\perp, \mathbf{p}_\perp, \tilde{z}, \delta, t). \tag{A15}$$

Multiplying Eq. (A1) by $\mathbf{x}_\perp$ and using integration by parts yields

$$\frac{d\mathbf{D}}{dt} = \frac{1}{\gamma m}\mathbf{P}. \tag{A16}$$

The key to obtaining (A16) is to notice that the integral of all terms proportional to $\partial F/\partial\mathbf{p}$ vanishes, since the coefficients of these terms do not depend on $\mathbf{p}$. Multiplying Eq. (A1) by $\mathbf{p}$ and proceeding similarly gives

$$\frac{d\mathbf{P}}{dt} = -\frac{q}{\gamma^2}\int d^2x_\perp d^2p_\perp F(\mathbf{x}_\perp, \mathbf{p}_\perp, \tilde{z}, \delta, t)\nabla\Phi(\mathbf{x}_\perp, \tilde{z}, t) - q\hat{x}k_x D_x(\tilde{z}, \delta, t) - q\hat{y}k_y D_y(\tilde{z}, \delta, t) + q[\hat{x}\mathcal{E}_x(\tilde{z}, t) + \hat{y}\mathcal{E}_y(\tilde{z}, t)]\Psi_0(\tilde{z}, \delta). \tag{A17}$$

The first term on the right of (A17) is due to space charge,

$$\mathbf{T}_{\text{sc}}(\tilde{z}, \delta, t) \equiv -\frac{q}{\gamma^2}\int d^2x_\perp d^2p_\perp F(\mathbf{x}_\perp, \mathbf{p}_\perp, \tilde{z}, \delta, t) \times \nabla\Phi(\mathbf{x}_\perp, \tilde{z}, t). \tag{A18}$$

The terms on the second and third lines are variants of well-known expressions, see, e.g., [56]. However, we have been somewhat sloppy with the δ dependence in the terms proportional to k_x and k_y. To include these terms to leading order, as well as the effects of closed orbit curvature and to change the timelike variable to θ, the reader only needs to check that the head-tail phase shifts are appropriate in the final equations. The point here is to deal with $\mathbf{T}_{\text{sc}}$; the aforementioned subtleties will be neglected.

To continue, notice that the integration with respect to $\mathbf{p}_\perp$ in Eq. (A18) affects only F so we may consider

$$\hat{F}(\mathbf{x}_\perp, \tilde{z}, \delta, t) = \int d^2p_\perp F(\mathbf{x}_\perp, \mathbf{p}_\perp, \tilde{z}, \delta, t).$$

We will now employ first order perturbation theory with $\hat{F} = R_0(\mathbf{x}_\perp, \tilde{z})\Psi_0(\tilde{z}, \delta) + \hat{F}_1(\mathbf{x}_\perp, \tilde{z}, \delta, t)$. Splitting the unperturbed distribution into this product form assumes that the transverse motion does not influence the longitudinal motion. Substituting the perturbation in Eq. (A18)

and using (A11)

$$\mathbf{T}_{\rm sc}(\tilde{z},\delta,t) = +\kappa\int d^2x'_\perp \rho_1(x'_\perp,\tilde{z},t)\int d^2x_\perp \frac{\mathbf{x}_\perp-\mathbf{x}'_\perp}{|\mathbf{x}_\perp-\mathbf{x}'_\perp|^2}\hat{F}_0(\mathbf{x}_\perp,\tilde{z},\delta) + \kappa\int d^2x_\perp \hat{F}_1(x_\perp,\tilde{z},\delta,t)\int d^2x'_\perp \frac{\mathbf{x}_\perp-\mathbf{x}'_\perp}{|\mathbf{x}_\perp-\mathbf{x}'_\perp|^2}\rho_0(\mathbf{x}'_\perp,\tilde{z}), \tag{A19}$$

where $\kappa = q/2\pi\epsilon_0\gamma^2$. The zeroth order terms are neglected, but vanish identically when the full equation is considered. The second order terms have been dropped. The next assumption is to take a uniform, elliptical density for the unperturbed distribution.

$$R_0(x,y,\tilde{z}) = \begin{cases} \frac{1}{\pi a_x a_y} & \text{if } \frac{x^2}{a_x^2}+\frac{y^2}{a_y^2}<1, \\ 0 & \text{otherwise.}\end{cases} \tag{A20}$$

Strictly speaking a_x and a_y should vary with $\tilde{z}$ due to the variation in space-charge defocusing along the bunch. Substituting this expression into (A19) and noticing that F_1 is zero for $x^2/a_x^2 + y^2/a_y^2 > 1$ gives

$$\mathbf{T}_{\rm sc}(\tilde{z},\delta,t) = -\kappa\int d^2x'_\perp \rho_1(x'_\perp,\tilde{z},t)\frac{(x'/a_x,y'/a_y)}{a_x+a_y}\Psi_0(\tilde{z},\delta) + \kappa\int d^2x_\perp \hat{F}_1(x_\perp,\tilde{z},\delta,t)\frac{(x/a_x,y/a_y)}{a_x+a_y}\int d\delta'\Psi_0(\tilde{z},\delta'). \tag{A21}$$

Substituting the definition for D and taking only the x component gives

$$T_{x,\rm sc}(\tilde{z},\delta,t) = \kappa_x D_x(\tilde{z},\delta,t)\int d\delta\Psi_0(\tilde{z},\delta) - \kappa_x\Psi_0(\tilde{z},\delta)\int d\delta D_x(\tilde{z},\delta,t), \tag{A22}$$

where $\kappa_x = \kappa/(a_x^2 + a_x a_y)$ and similarly for D_y To obtain the space-charge term in Eq. (10) notice that $y_p \equiv D_y/\Psi_0$ and that Y is obtained by heterodyning y_p. Therefore, define $X(\tilde{z},\delta,t) \equiv D_x/\Psi_0$. Since $d\Psi_0/dt \equiv 0$ the equation for X is given by

$$\frac{d^2X}{dt^2} = -\frac{qk_x}{\gamma m}X + \frac{q\mathcal{E}_x(\tilde{z},t)}{\gamma m} + \frac{\kappa_x}{\gamma m}X(\tilde{z},\delta,t)\int d\delta_1\Psi_0(\tilde{z},\delta_1) - \frac{\kappa_x}{\gamma m}\int d\delta_1 X(\tilde{z},\delta_1,t)\Psi_0(\tilde{z},\delta_1). \tag{A23}$$

Using a square well longitudinal potential, changing variables, and taking a single betatron sideband in Eq. (A23) gives Eq. (11), concluding the derivation.

*Electronic address: mmb@bnl.gov

[1] D. Neuffer, E. Colton, D. Fitzgerald, T. Hardek, R. Hutson, R. Macek, M. Plum, H. Thiessen, and T. S. Wang, Nucl. Instrum. Methods Phys. Res., Sect. A **321**, 1 (1992).

[2] M. A. Plum, D. H. Fitzgerald, D. Johnson, J. Langenbrunner, R. J. Macek, F. Merril, P. Morton, B. Prichard, O. Sander, M. Shulze, H. A. Thiessen, T. S. Wang, and C. A. Wilkinson, in *Proceedings of the PAC97, Vancouver* (IEEE, Piscataway, NJ, 1997), p. 1611.

[3] R. Macek, in *Workshop on Space Charge Physics in High Intensity Hadron Rings*, AIP Conf. Proc. No. 448 (AIP, New York, 1998), p. 116.

[4] M. Blaskiewicz, in *Workshop on Instabilities of High Intensity Hadron Beams in Rings*, AIP Conf. Proc. No. 496 (AIP, New York, 1999), p. 321.

[5] H. G. Hereward, CERN Report No. 71-15, 1971.

[6] E. Keil and B. Zotter, CERN Report No. CERN/ISR-TH/71-58, 1971.

[7] M. Izawa, Y. Sato, and T. Toyomasu, Phys. Rev. Lett. **74**, 5044 (1995).

[8] T. Holmquist and J. Rogers, Phys. Rev. Lett. **79**, 3186 (1997).

[9] H. Fukuma, K. Akai, N. Akasaka, K. Bane, K. Egawa, A. Enomoto, J. W. Flanagan, Y. Funakoshi, K. Furukawa, K. Hayashi, S. Hiramatsu, H. Hisamatsu, K. Hosoyama, N. Huang, T. Ieiri, N. Iida, T. Kamitani, K. Kanazawa, S. Kato, K. Kikuchi, E. Kikutani, H. Koiso, T. Kubo, S. Kurokawa, T. Mitsuhashi, M. Masuzawa, T. Matsumoto, S. Michizono, T. Mimashi, T. Nakamura, Y. Ogawa, K. Ohmi, Y. Ohnishi, S. Ohsawa, N. Ohuchi, K. Oide, E. A. Perevedentsev, D. Pestrikov, K. Satoh, M. Suetake, Y. Suetsugu, T. Suwada, F. Takasaki, M. Tanaka, M. Tawada, M. Tejima, M. Tobiyama, T. Tsuboyama, N. Yamamoto, M. Yoshida, S. Yoshimoto, C. H. Yu, F. Zimmermann, and S. Olsen, in *Proceedings of the EPAC2000, Vienna, Austria*, edited by M. Regler (European Physical Society, Geneva, 2000), p. 1122.

[10] G. Rumolo, F. Zimmermann, H. Fukuma, and K. Ohmi, in *Proceedings of the PAC01, Chicago* (IEEE, Piscataway, NJ, 2001), p. 1889.

[11] A. Kulikov, A. S. Fisher, S. Heifets, J. T. Seeman, M. Sullivan, U. Weinands, and W. Kozanecki, in *Proceedings of the PAC01, Chicago* (Ref. [10]), p. 1903.

[12] F. Zimmermann, in *Proceedings of the PAC01, Chicago* (Ref. [10]), p. 666.

[13] K. Ohmi and F. Zimmermann, Phys. Rev. Lett. **85**, 3821 (2000).
[14] K. Ohmi, Phys. Rev. Lett. **75**, 1526 (1995).
[15] K. Ohmi, F. Zimmermann, and E. Perevedentsev, Phys. Rev. E **65**, 016502 (2001).
[16] E. Perevedentsev, CERN Report No. CERN-2002-001, 2002, p. 171.
[17] R. Cappi, M. Giovannozzi, E. Metral, G. Metral, and F. Zimmermann, in *Proceedings of the PAC01, Chicago* (Ref. [10]], p. 682.
[18] G. Arduini, V. Baglin, O. Bruning, R. Cappi, F. Caspers, P. Collier, I. R. Collins, K. Cornelis, R. Garoby, O. Gröbner, B. Henrist, N. Hilleret, W. Holfle, J. M. Jimenez, J. M. Laurent, T. Linnecar, E. Mercier, M. Pivi, F. Ruggiero, G. Rumolo, C. Scheuerlein, J. Tuckmantel, L. Vos, and F. Zimmermann, in *Proceedings of the EPAC2000, Vienna, Austria* (Ref. [9]), p. 259.
[19] B. V. Chirikov, Sov. At. Energy **19**, 239 (1965).
[20] L. J. Laslett, A. M. Sessler, and D. Möhl, Nucl. Instrum. Methods **121**, 517 (1974).
[21] R. C. Davidson, H. Qin, and P. H. Stoltz, Phys. Rev. ST Accel. Beams **2**, 054401 (1999).
[22] M. Blaskiewicz, in *Proceedings of the PAC99, New York* (IEEE, Piscataway, NJ, 1999), p. 1611.
[23] R. Macek, in *Proceedings of the 8th ICFA Beam Dynamics Mini-workshop, Santa Fe, 2000*, available online at http://www.aps.anl.gov/conferences/icfa/two-stream.html
[24] K. Ohmi, T. Toyama, and C. Ohmori, Phys. Rev. ST Accel. Beams **5**, 114402 (2002).
[25] R. C. Davidson, H. Qin, and P. J. Channell, Phys. Rev. ST Accel. Beams **2**, 074401 (1999).
[26] H. Qin, R. C. Davidson, E. Startsev, and W. W. Lee, in *Proceedings of the PAC01, Chicago* (Ref. [10]), p. 693.
[27] M. Blaskiewicz, in *Proceedings of the 8th ICFA Beam Dynamics Mini-workshop, Santa Fe, 2000* (Ref. [23]).
[28] T. S. Wang, P. J. Channell, R. Macek, and R. C. Davidson, in *Proceedings of the PAC01, Chicago* (Ref. [10]), p. 704.
[29] T. S. F. Wang, P. J. Channell, R. J. Macek, and R. Davidson (to be published).
[30] P. J. Channell, Phys. Rev. ST Accel. Beams **5**, 114401 (2002).
[31] K. Y. Ng, D. Wildman, M. Popovic, A. Browman, D. Fitzgerald, R. Macek, M. Plum, and T. Spickermann, in *Proceedings of the PAC01, Chicago* (Ref. [10]), p. 2890.
[32] R. J. Macek, in *Proceedings of the PAC01, Chicago* (Ref. [10]), p. 688.
[33] R. J. Macek, in Proceedings of the ICANS-XV, KEK, Tsukuba, Japan, 2000 (to be published).
[34] A. Browman, in *Proceedings of the 8th ICFA Beam Dynamics Mini-workshop, Santa Fe, 2000* (Ref. [23]).
[35] M. Plum, PSR Technical Note No. PSR-94-001, 1994.
[36] G. V. Stupakov, LHC Project Report No. 141, 1997.
[37] M. A. Furman and G. Lambertson, in *Proceedings of the International Workshop on Multibunch Instabilities in Future Electron and Positron Accelerators MBI97, Tsukuba, Japan, 1997*, edited by Y. H. Chin (KEK Report No. 97-17, 1997), p. 170.
[38] O. Gröbner, in *Proceedings of the PAC97, Vancouver* (Ref. [2]).
[39] V. Danilov, J. Galambos, D. Jeon, J. Holmes, D. Olsen, D. Fitzgerald, R. Macek, M. Plum, J. Griffin, and A. Burov, in *Proceedings of the PAC99, New York* (Ref. [22]), p. 1201.
[40] M. Pivi and M. A. Furman, in *Proceedings of the 8th ICFA Beam Dynamics Mini-workshop, Santa Fe, 2000* (Ref. [23]).
[41] M. Pivi and M. A. Furman, CERN Report No. CERN/2002/001, 2002.
[42] M. Pivi and M. A. Furman, Phys. Rev. ST Accel. Beams **5**, 124404 (2002).
[43] B. Henrist, N. Hilleret, C. Scheuerlein, M. Taborelli, and G. Vorlaufer, in *Proceedings of the 8th EPAC02, Paris* (European Physical Society, Geneva, 2002), p. 2553.
[44] Y. Kijima, S. Mitsunobu, T. Furuya, and R. Noer, in *Proceedings of the 10th Workshop on RF Superconductivity*, contribution PT027, available online at http://conference.kek.jp/SRF2001/.
[45] Y. Chin, CERN Report No. CERN/LEP-TH/88-05, 1988, and references therein.
[46] We use the eispack routine cg. It is available online at http://www.netlib.org.
[47] M. Blaskiewicz, Phys. Rev. ST Accel. Beams **1**, 044201 (1998).
[48] V. V. Danilov and E. A. Perevedentsev, in *Proceedings of the 15th ICHEA, Hamburg, 1992* (World Scientific, Singapore, 1992), p. 1163.
[49] M. Blaskiewicz, in *Proceedings of the EPAC 2000, Vienna, Austria* (Ref. [9]).
[50] Y. Chin and H. Tsutsui, in *Proceedings of the PAC97, Vancouver* (Ref. [2]), p. 1545.
[51] H. Goldstein, *Classical Mechanics* (Addison-Wesley, Reading, MA, 1981.
[52] M. Blaskiewicz, Phys. Rev. ST Accel. Beams **4**, 044202 (2001).
[53] Strictly speaking, ω_β should include the effects of image currents in the bending magnets and other dc terms. This will not be an issue as long as the coherent tune shift neglects these dc terms too.
[54] S. S. Kurennoy, in *Workshop on Instabilities of High Intensity Hadron Beams in Rings*, AIP Conf. Proc. No. 496 (Ref. [4]), p. 361.
[55] Computer codes using this approximation or close variants include J. Galambos, ORBIT, ORNL; A. Luccio, ORBIT, BNL; F. W. Jones, ACCSIM, TRIUMF; S. Machida, SIMPSONS, KEK; C. R. Prior, TRACK3D, RAL.
[56] F. Ruggiero, Part. Accel. **20**, 45 (1986).